Journal of the Mechanics and Physics of Solids 144 (2020) 104114

Contents lists available at ScienceDirect

Journal of the Mechanics and Physics of Solids

journal homepage: www.elsevier.com/locate/jmps

Finite-strain scale-free phase-field approach to multivariant martensitic phase transformations with stress-dependent effective thresholds

Hamed Babaei [a], Valery I. Levitas [a,b,c,*]

[a] Department of Aerospace Engineering, Iowa State University, Ames, IA 50011, USA
[b] Departments of Mechanical Engineering, Iowa State University, Ames, IA 50011, USA
[c] Ames Laboratory, Division of Materials Science and Engineering, Ames, IA 50011, USA

ARTICLE INFO

Article history:
Received 13 July 2020
Revised 5 August 2020
Accepted 12 August 2020
Available online 15 August 2020

Keywords:
Finite strain
Scale-free phase-field approach
Martensitic phase transformation
PT conditions
Stress-dependent effective threshold

ABSTRACT

A scale-free phase-field model for martensitic phase transformations (PTs) at finite strains is developed as an essential generalization of small-strain models in Levitas et al. (2004) and Idesman et al. (2005). The theory includes finite elastic and transformational strains and rotations as well as anisotropic and different elastic properties of phases. The gradient energy term is excluded, and the model is applicable for any scale greater than 100 nm. The model tracks finite-width interfaces between austenite and the mixture of martensitic variants only; volume fractions of martensitic variants are the internal variables rather than order parameters. The concept of the effective threshold for the driving force is introduced, which can be either positive (e.g., due to interface friction) or negative (e.g., due to defects and stress concentrators promoting PTs). To reproduce PT conditions obtained from experiments or atomistic simulations under general stress tensor, the effective threshold depends on the stress tensor components. Material parameters are calibrated for martensitic PT between single crystalline cubic Si I and tetragonal Si II phases, which has large transformation strains ($\boldsymbol{\varepsilon}_{t1} = 0.1753; \boldsymbol{\varepsilon}_{t2} = 0.1753; \boldsymbol{\varepsilon}_{t3} = -0.447$). Finite element algorithms and numerical procedures are implemented in the code deal.II. Multiple 3D problems are solved to study the effect of mesh size, holding time during quasi-static loading, and strain rate on the multivariant microstructure evolution in Si I $\rightarrow$ Si II PT under uniaxial and hydrostatic loadings. The solution exhibits significant lattice rotations both in Si I and Si II, reproducing the appearance of diffuse grain boundaries in Si I and Si II and transforming them in polycrystals, which corresponds to known experiments. While finer mesh can produce a more detailed microstructure, the solution becomes practically mesh-independent after the mesh size is 80 times smaller than the sample size. When approaching the stationary solution, rough mesh leads to convergence to the correct microstructure faster than the fine mesh, because it neglects fine details in the microstructure. In some regions, reverse PT occurs at continuous compression, despite large transformation hysteresis. For most stationary interfaces, local thermodynamic equilibrium conditions (thermodynamic driving force for the interface motion equal to the effective threshold) are satisfied.

* Corresponding author.
E-mail address: vlevitas@iastate.edu (V.I. Levitas).

https://doi.org/10.1016/j.jmps.2020.104114
0022-5096/

1. Introduction

Martensitic (diffusionless) phase transformation (PT) between the austenite and martensite is one of the essential deformation mechanisms in crystalline materials, such as metals, ceramics, geological materials, and shape memory alloys. The physical properties of the materials undergoing PT are highly influenced by the martensitic microstructure evolution, which itself is affected by external loading conditions as well as crystal and defect structures. Therefore, because the formation of the desirable martensitic microstructure is one of the main goals of computational material design, developing a proper modeling approach is essential to obtain a comprehensive understanding of all the effects of various parameters on the martensitic microstructure evolution. Different modeling approaches to martensitic PTs in elastic materials have been developed by researchers as follows:

(a) Elastoplastic models (Beissel and Belytschko, 1996; Jiang et al., 2017a; 2017b; Shaw, 2000). In these models, strain localization resulted from strain softening is used to resemble microstructure observed during PTs. Although several model problems on nucleation, microstructure formation and propagation in viscoplastic materials (Beissel and Belytschko, 1996) and polycrystalline NiTi Shaw (2000) were studied using elastoplastic models, as they do not take into account thermomechanics and crystallography of multivariant martensitic PTs, they cannot describe certain essential features of these phenomena.

(b) Thermomechanical phenomenological models (Arghavani et al., 2010; Lagoudas et al., 2012; Panico and Brinson, 2007; Zaki and Moumni, 2007), and others). Based on the treatment of martensitic PTs as a mixture of different phases with varying volume fractions, these models ignore the discrete nature of microstructure and exhibit a continuous smooth distribution of volume fraction of martensitic variants martensite or martensite. Such a smeared description of microstructure results from the strain hardening in the local constitutive equations, which in turn prevents strain localization.

(c) Nanoscale phase-field/Ginzburg-Landau models (Artemev et al., 2001; 2000; Idesman et al., 2008; Wang and Khachaturyan, 1997; Zhu et al., 2017), including finite strain models (Basak and Levitas, 2018; Clayton and Knap, 2011; Levitas et al., 2009; 2013). At the nanoscale, the phase-field approach can describe the formation of discrete nanostructure of austenite and m martensitic variants effectively without a need for the development of a complicated computational algorithm to track sharp martensitic interfaces. Diffuse (finite-width) martensitic interfaces appear as the solution of the Ginzburg-Landau evolution equation; the width of the interfaces is controlled by the gradient energy term and the double-well barrier. However, the main problem with these models is that because the width of the martensitic interface is ~ 1 nm and we need at least 3–5 computational element within the interface (Chen and Shen, 1998), we are computationally limited to single- or poly-nanocrystals, while the grain size for most engineering materials is 10–1000 μm.

(d) Phase-field approaches that use volume fractions of all phases as order parameters (Steinbach, 2009; Steinbach et al., 1996), including finite-strain formulations (Schneider et al., 2015; Tuma and Stupkiewicz, 2016; Tuma et al., 2016). The sum of all order parameters is equal to unity, which imposes some problems in theory reviewed in Tóth et al. (2015),Levitas and Roy (2016). While these theories do not satisfy conditions for nanoscale interpolation functions (Levitas, 2018; Levitas and Preston, 2002a; 2002b), they are broadly applied to nanoscale problems. In other works, the width of the interface is artificially increased from $\sim 1nm$ to $\sim 1\mu m$ (Steinbach and Apel, 2006). As it is discussed in Esfahani et al. (2018), this leads to the reduction in the magnitude of the double-well barrier, stress and temperature hysteresis by the same proportion ($\sim 10^3$) and, consequently, to significant changes in macroscopic stress-strain curves, and possible multiple artificial nucleations during the simulations due to a stress or temperature heterogeneities.

(e) Microscale (or scale-free) phase-field model(Esfahani et al., 2020; 2018; Idesman et al., 2005; Levitas et al., 2004). This approach synergistically combines some features of nanoscale phase-field models with thermomechanical phenomenological models and can reproduce discrete multivariant MM evolution in single- and poly-crystals at scales greater than 100 nm without any upper bound. While the volume fraction of martensite c is considered as the order parameter responsible for the material instability, the volume fraction of martensitic variants c_i are just internal variables. After including strain softening due to austenite↔martensite PTs in the constitutive equations, similar to the Ginzburg-Landau models, a localized discrete austenite - multivariant MM (consisting of the mixture of martensitic variants) is formed as opposed to the thermomechanical phenomenological models with a smeared and continuous distribution of martensite. However, the gradient energy term is dropped, making this model a scale-free one. It includes the surface energy in an average sense through introducing an interaction term between phases in the thermodynamic potential. Discussion on dropping gradient energy is presented in Esfahani et al. (2018) and will not be repeated here.

One of the problems in the model (Esfahani et al., 2018; Idesman et al., 2005; Levitas et al., 2004) is that it is developed for the small strains only, while for PTs in many engineering materials transformations strains are finite. All computational applications of the model are limited to 2D formulations. Here, we generalized this model for finite elastic and transformation strains and lattice rotations, as well as for anisotropic and different elastic properties of phases, and solve 3D problems.

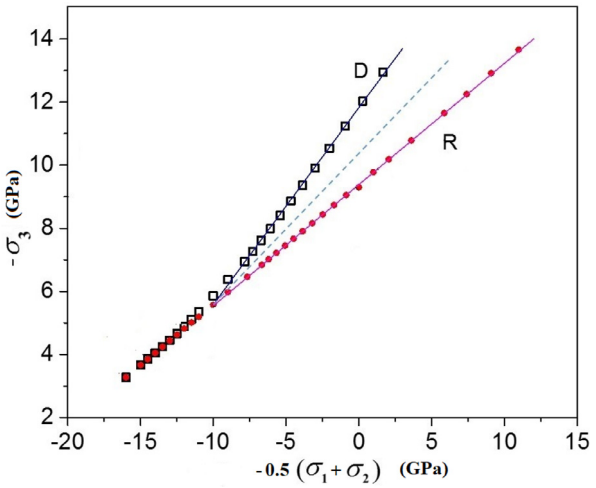

Fig. 1. Relationships between stresses σ_3 and $0.5(\sigma_1+\sigma_2)$ for PT criteria for direct and reverse Si I↔Si II PTs for the variant 1 with compressive transformation strain along the direction 3 and equal transformation strains along the directions 1 and 2. The dashed line is the schematic phase equilibrium line. When two instability lines merge, no energy barrier between phases exists, which leads to a unique homogeneous and hysteresis-free first-order Si I↔Si II PT. Obtained using molecular dynamics simulations in Levitas et al. (2017b).

The second problem is more challenging. The crystal lattice instability conditions (which are PT criteria for a perfect crystal) for the PTs between semiconducting cubic diamond Si I and metallic $\beta-Sn$ Si II under the action of all six components of the stress tensor were found with the help of molecular dynamics simulations in Levitas et al. (2017a,b). For direct Si I $\rightarrow$ Si II PT, the lattice instability criterion was confirmed by the first-principle simulations in Zarkevich et al. (2018) and Chen et al. (2020). These criteria are linear functions of the Cauchy stress components normal to the cubic faces of Si I, σ_i, and are weakly dependent on the shear stresses (Fig. 1. Consequently, the lattice instability criteria can be visualized in a 3D stress space σ_i as two planes, one for Si I $\rightarrow$ Si II PT and another for Si II $\rightarrow$ Si I PT. The key problem is that these planes are not parallel, intersect and coincide along a line. After the intersection of these planes, they coincide with the phase equilibrium condition. These could not be described by previously existing nanoscale PFAs. A new nanoscale PFA was developed in Levitas (2018) that satisfies the PT criteria obtained by atomistic simulations. This was particularly achieved by introducing new interpolation functions of the order parameter for the transformation strain tensor, different for each independent component. This theory was applied for the finite element method (FEM) solution of several material problems under complex loading in Babaei and Levitas (2018),Babaei and Levitas (2019). It is clear that for real defective crystal, PT conditions will be different, but defects cannot make PT planes in the stress space parallel. Indeed, single dislocations slightly change PT conditions under uniaxial compression but did not change the coinciding portion of PT planes; see Babaei and Levitas (2019). Thus, we need to develop a scale-free theory generalizing theories in Levitas et al. (2004), Idesman et al. (2005) and Esfahani et al. (2018) for finite strain and for PT conditions that are not parallel in the 3D stress space. Since we want to use the simple mixture theory, we cannot use complex nonlinear interpolation functions for the transformation strain tensor, as we did for the nanoscale model in Levitas (2018). The PT conditions in Levitas et al. (2004), Idesman et al. (2005) and Esfahani et al. (2018) have the form $X_{i0}=k_{i0}$, where X_{i0} is the thermodynamic driving force for the austenite $(\mathsf{A})\rightarrow$ ith martensitic variant M_i PT and $k_{i0}>0$ is the athermal threshold or athermal interface friction. Usually, k_{i0} was considered to be the same for direct and reverse PTs and constant or function of the volume fraction of the product phase. The only way to incorporate non-parallel PT planes in the stress space is to assume that k_{i0} depends on the Cauchy stress components normal to the cubic faces of Si I, σ_i. This is done in the paper and calibrated by known PT conditions.

The third unexpected problem is that due to large transformation strains, the slopes of the phase equilibrium lines $X_{i0}=0$ for direct (at $c_i=0$) and reverse (at $c_i=1$) PTs are quite different and they intersect the PT initiation line $X_{i0}=k_{i0}$ for direct PT and $X_{i0}=-k_{i0}$ for reverse PT (Fig. 2). This means that for large compressive stresses $0.5(\sigma_1+\sigma_2)$, $\mathsf{A}\rightarrow\mathsf{M}_i$ PT starts in the region of stability of A, $k_{i0}<0$ and dissipation rate $k_{i0}\dot{c}_i<0$, i.e., there is a formal violation of the second law of thermodynamics. This issue is discussed in detail. While it sounds catastrophic, there are many experimental results for different material systems demonstrating that under plastic straining PT may occur at a pressure well below than the phase equilibrium pressure (Blank and Estrin, 2013; Gao et al., 2019; Pandey and Levitas, 2020). Such a counterintuitive behavior was explained in Levitas (2004), Javanbakht and Levitas (2018), Javanbakht and Levitas (2015), Levitas et al. (2018)and Esfahani et al. (2020) by strong stress tensor concentration produced by defects induced by plastic deformation, e.g., dislocation pileups. This means that in the framework of more general theory with defects, such behavior is thermodynamically consistent. That is why we accept that within our theory, k_{i-0} effectively includes the effect of the defect-induced stress concentrators, and it may be negative for some combination of stresses, while the net thermodynamic driving force $X_{net}=X_{i0}-k_{i-0}>0$. To include this possibility, k_{i-0} is called the effective threshold instead of a positive athermal threshold.

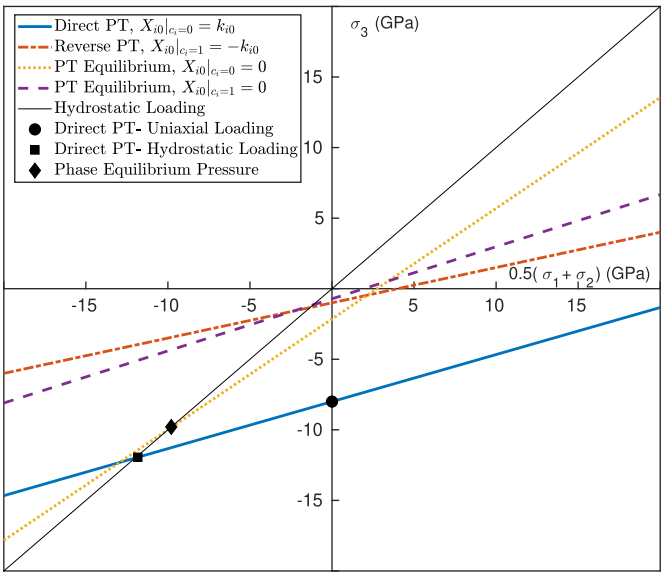

Fig. 2. Relative positions of the lines for initiation of the direct and reverse PTs ($X_{i0} = k_{i-0}$ at $c_i = 0$ and $X_{i0} = -k_{i-0}$ at $c_i = 1$, respectively), phase equilibrium lines $X_{0i} = 0$ for $c = 0$ and $c = 1$, hydrostatic loading line $\sigma_1 = \sigma_2 = \sigma_3$, empirical uniaxial and hydrostatic instability points and phase equilibrium pressure used for calibration of PT conditions.

In continuum modeling of PTs in Si I, including phenomenological (Budnitzki and Kuna, 2016) and nanoscale PFA (Babaei and Levitas, 2018; 2019; Levitas, 2018) treatments, Si II was considered as a single variant. However, twinned (i.e., multivariant) Si II was recently observed in Popov et al. (2015) in a hydrostatic loading experiment during Si I → Si II PT utilizing Laue diffraction. Here, we will present the first modeling and simulation results for multivariant Si I → Si II PT.

The paper is organized as follows. The large-strain PFA model is presented in Section 2. The stress tensor and volume fraction of phases dependent effective threshold, and consequently, stress hysteresis is introduced and connected to PT conditions for direct and reverse PTs in Section 3. Parameter identification for PT Si I → Si II is presented in Section 4. It involves discussion on and acceptance of the negative effective threshold. Problem formulations on uniaxial compression of a Si single crystal are formulated in Section 5 and a typical 3D solution is presented. Computational challenges are related to large complete transformation strains (−0.447), which varies from zero to its maximum magnitude within numerous phase interfaces with a width of a single finite element. The effect of various parameters on the microstructure evolution is studied in Section 6. The effect of the FEM mesh size is analyzed in Section 6.1. It is shown that although finer mesh can produce a more detailed microstructure, the solution is getting practically mesh-independent after the mesh size is 80 times smaller than the sample size. For solutions close to the stationary ones, solutions with rough mesh converge to correct microstructure faster than with the fine mesh, because it neglects fine details in microstructure from the beginning. Evolution of rotation of the crystal lattices of Si I and Si II is studied in Section 6.2. It appears that finite strain formulation allowed us to reproduce the formation of grains and polycrystalline structure both in Si I and Si II from initial single-crystal Si I. The effect of the holding time during the quasi-static loading is elaborated in Section 6.3. The effect of the strain rate is studied in Section 6.4. It is found in Section 6.5 that for the majority of the stationary interfaces, the local thermodynamic equilibrium conditions (thermodynamic driving force for the interface motion equal to the effective threshold) are met. The solution for the PT under hydrostatic loading is presented in Section 6.6. Section 7 contains concluding remarks.

Vectors and tensors are designated with boldface symbols. We designate contractions of tensors $\boldsymbol{A} = \{A_{ij}\}$ and $\boldsymbol{B} = \{B_{ji}\}$ over one and two indices as $\boldsymbol{A}\cdot\boldsymbol{B} = \{A_{ij}B_{jk}\}$ and $\boldsymbol{A}:\boldsymbol{B} = A_{ij}B_{ji}$. The transpose of $\boldsymbol{A}$ is $\boldsymbol{A}^T$; $\boldsymbol{I}$ is the unit tensor; $\boldsymbol{\nabla}_0$ is the gradient operator in the undeformed state.

2. Model description

Here, we discuss our phenomenological microscale model for multivariant martensitic PT in elastic materials. A typical martensitic entity consists of numerous alternating martensitic variants with planar interfaces, most often twin-related. Because the width of each martensitic variant is $d \simeq 10\,\text{nm}$, it would be computationally impractical to model each of thousands of twinned layers of martensitic variants in mm-sized or larger samples while resolving the interface between variants. Therefore, because our goal is to develop a proper model for microscale or larger samples that does not aim at the exact resolution of martensite-martensite interfaces, we consider a minimum size for our representative volume as $l \simeq 10d \simeq 100\,\text{nm}$, in which we have a sufficient number of layers of m martensitic variants.

2.1. Kinematics

The motion of an elastic body undergoing PTs can be expressed by a continuous function $\boldsymbol{r} = \boldsymbol{r}(\boldsymbol{r}_0, t)$, where $\boldsymbol{r}_0$ and $\boldsymbol{r}$ are the positions of material points in the undeformed Ω_0 and the deformed Ω configurations, respectively; t is the time. The multiplicative decomposition of the deformation gradient into the elastic part and symmetric transformation part is expressed as

$$\boldsymbol{F} := \nabla_0 \boldsymbol{r} = \boldsymbol{F}_e \cdot \boldsymbol{F}_t; \qquad \boldsymbol{F}_t = \boldsymbol{F}_t^T. \tag{1}$$

In the intermediate configuration Ω_t, obtained by applying the transformation deformation $\boldsymbol{F}_t$ to points in the reference configuration Ω_0, the crystal lattice represents the stress-free product phase or intermediate phase along the transformation path from the lattice of parent phase to that of product phase. This configuration is obtained through the release of elastic stresses down to zero from the actual configuration Ω. Rigid-body rotations are excluded from $\boldsymbol{F}_t$; that is why the question of the objectivity of the constitutive equations under superposition of the rigid-body rotations in Ω_t is not considered. The transformation deformation gradient is expressed as

$$\boldsymbol{F}_t = \boldsymbol{I} + \boldsymbol{\varepsilon}_t = \boldsymbol{I} + \sum_{i=1}^{m} \boldsymbol{\varepsilon}_{ti} c_i, \tag{2}$$

where $\boldsymbol{\varepsilon}_{ti}$ indicates the Bain strain tensor for the transformation of a crystal lattice of austenite to the ith martensitic variant, and $\boldsymbol{\varepsilon}_t$ is the transformation strain in the martensitic mixture. Also, c_0 and c_i $(i = 1, 2, \ldots, m)$ are the volume fraction of the austenite and the ith martensitic variant and $c = \sum_{i=1}^{m} c_i$ is the volume fraction of martensite (M); therefore, $\sum_{i=0}^{m} c_i = c_0 + c = 1$. For small strain, a more precise equation for the eigen strain of the mixture, which includes stress localization matrices, was derived in Mandel (1966). For large strain, a much more complex rate equation is presented in Levitas (1996). These more precise equations take into account that for the macroscopically stress-free state, heterogeneous internal elastic strains (and stresses) exist in a mixture. If internal elastic strain neglected, Eq. (2) is the exact equation of the theory of microheterogeneous materials.

The Lagrangian total, elastic, and transformation strains are given respectively by

$$\boldsymbol{E} = \frac{1}{2}(\boldsymbol{F}^t \cdot \boldsymbol{F} - \boldsymbol{I}); \quad \boldsymbol{E}_e = \frac{1}{2}(\boldsymbol{F}_e^t \cdot \boldsymbol{F}_e - \boldsymbol{I}); \quad \boldsymbol{E}_t = \frac{1}{2}(\boldsymbol{F}_t \cdot \boldsymbol{F}_t - \boldsymbol{I}); \qquad \boldsymbol{E} = \boldsymbol{F}_t \cdot \boldsymbol{E}_e \cdot \boldsymbol{F}_t + \boldsymbol{E}_t. \tag{3}$$

The Jacobian determinants that characterize the ratios of volumes V and mass densities ρ in the corresponding configurations, are

$$J = \frac{dV}{dV_0} = \frac{\rho_0}{\rho} = det\boldsymbol{F}; \quad J_t := \frac{dV_t}{dV_0} = \frac{\rho_0}{\rho_t} = det\boldsymbol{F}_t; \quad J_e := \frac{dV}{dV_t} = \frac{\rho_t}{\rho} = det\boldsymbol{F}_e \;\Rightarrow J = J_t J_e. \tag{4}$$

2.2. Free energy and dissipation inequality

The Helmholtz free energy ψ per unit undeformed volume in Ω_0 of the mixture of austenite and m martensitic variants is assumed to be in the form

$$\psi(\boldsymbol{F}_e, c_i, \theta) = J_t \psi^e(\boldsymbol{F}_e, c_i) + \psi^\theta(\theta, c_i) + \psi^{in}(c_i), \tag{5}$$

where ψ^e is the elastic energy per unit volume in the configuration Ω_t, in which the elasticity rule is defined in experiments; Jacobian J_t transformed it to the energy per unit volume in the configuration Ω_0; ψ_i^θ is the thermal energy, which includes the thermal driving force for the PT; θ is the temperature; ψ^{in} is the interaction energy which represents the contribution to the free energy of the mixture due to the interactions between austenite and all martensitic variants including the energy of internal stresses as well as the phase interface energy. It should be noted that since the simulations are done for stress-induced PTs at constant room temperature, the thermal expansion is neglected. It can be included in a traditional way if temperature varies.

The simplest elastic energy for an anisotropic crystal is expressed as

$$\psi^e = \frac{1}{2}\boldsymbol{E}_e : \boldsymbol{C} : \boldsymbol{E}_e = \frac{1}{2} C^{ijkl} E_e^{ij} E_e^{kl} = \frac{1}{2}\sum_{n=1}^{3}\left[\lambda^n (E_e{}^{nn})^2 + 2\mu^n E_e^{nn} E_e^{kk} + 4\nu^n E_e^{nk} E_e^{kn}\right]. \tag{6}$$

Note that higher-order elastic constants have been used for perfect Si I crystal, even up to fifth-degree (Chen et al., 2020), in order to describe behavior for elastic strains up to 0.35, including elastic lattice instabilities, and pressure up to 80 GPa. Here, we use the second-order elastic energy because firstly, for a microscale sample, which generally includes defects, the PT initiates at much smaller elastic strains ($<$ 0.1) and pressure ($<$ 12 GPa) compared to the perfect crystals, and secondly, only second-order elastic constants are known for Si II phase. The fourth rank elastic moduli for orthotropic materials with three orthogonal symmetry planes are considered in the local coordinate system related to a crystal lattice as

$$C^{ijkl} = \sum_{n=1}^{3}\left[\lambda^n \delta^{in}\delta^{jn}\delta^{kn}\delta^{ln} + \mu^n(\delta^{in}\delta^{jn}\delta^{kl} + \delta^{ij}\delta^{kn}\delta^{ln}) + \nu^n(\delta^{in}\delta^{jk}\delta^{ln} + \delta^{jn}\delta^{ik}\delta^{ln} + \delta^{in}\delta^{jl}\delta^{kn} + \delta^{jn}\delta^{il}\delta^{kn})\right], \tag{7}$$

where parameters λ^n, μ^n and ν^n can be expressed in terms of nine independent elastic constants, and δ^{ij} is the Kronecker delta. For tetragonal crystal lattice, two of the symmetry planes are equivalent. Therefore, $C^{11} = C^{22}$, $C^{13} = C^{23}$ and $C^{44} = C^{55}$, and consequently

$$\begin{aligned} \lambda^1 &= \lambda^2 = C^{11} - (C^{12} + 2C^{66}), \\ \lambda^3 &= C^{33} + C^{12} + 2C^{66} - 2(C^{13} + 2C^{44}), \\ 2\mu^1 &= 2\mu^2 = C^{12}, \quad 2\mu^3 = 2C^{13} - C^{12}, \\ 2\nu^1 &= 2\nu^2 = C^{66}, \quad 2\nu^3 = 2C^{44} - C^{66}. \end{aligned} \tag{8}$$

Besides, for the cubic crystal lattice, all three orthogonal symmetry planes are equivalent, resulting in $C^{11} = C^{22} = C^{33}$, $C^{13} = C^{23} = C^{13}$ and $C^{44} = C^{55} = C^{66}$, so that

$$\begin{aligned} \lambda^1 &= \lambda^2 = \lambda^3 = C^{11} - C^{12} - 2C^{44}, \\ 2\mu^1 &= 2\mu^2 = 2\mu^3 = C^{12}, \\ 2\nu^1 &= 2\nu^2 = 2\nu^3 = C^{44}. \end{aligned} \tag{9}$$

During the PT, the elastic constants λ^n, μ^n and ν^n for the three orthogonal directions are interpolated as

$$\lambda^n = \sum_{i=0}^{m} \lambda_i^n c_i; \quad \mu^n = \sum_{i=0}^{m} \mu_i^n c_i; \quad \nu^n = \sum_{i=0}^{m} \nu_i^n c_i, \tag{10}$$

with λ_i^n, μ_i^n, ν_i^n for the elastic constants of austenite ($i = 0$) and martensitic variants. More complex nonlinear relationship can be used from the theory of effective moduli of composite materials (Buryachenko, 2007).

The thermal part of the free energy is

$$\psi^\theta = \sum_{i=0}^{m} c_i \psi_i^\theta(\theta) = c_0 \psi_A^\theta(\theta) + c\psi_M^\theta(\theta), \tag{11}$$

where ψ_i^θ is the thermal energy of the ith phase. Because of the equivalence of the martensitic variants, their thermal energy is the same ($\psi_i^\theta = \psi_j^\theta = \psi_M^\theta$ for $i, j > 0$), therefore, ψ_A^θ and ψ_M^θ represent the thermal energy of austenite and martensite.

The interaction energy, which penalizes the surface energy of all interfaces, as well as the energy of internal stresses due to the lattice mismatch between austenite and martensitic variants, can be presented in the form (Idesman et al., 2005)

$$\psi^{in} = \mathcal{A} c c_0 + \sum_{i=1}^{m} \sum_{j=1}^{m} \mathcal{A}_{ij} c_i c_j \geq 0, \quad \mathcal{A} > 0, \quad \mathcal{A}_{ij} \geq 0, \quad \mathcal{A}_{ii} = 0, \tag{12}$$

where $\mathcal{A}$ and $\mathcal{A}_{ij}$ are the material parameters for the interaction between austenite and all martensitic variants, and the interaction between martensitic variants themselves, respectively.

Utilizing the first two laws of thermodynamics in the form of Clausius-Planck inequality (since temperature gradient is zero), one can obtain the following expression for the dissipation inequality

$$D = \boldsymbol{P}^T \boldsymbol{:} \dot{\boldsymbol{F}} - \dot{\psi} - s\dot{\theta} \geq 0, \tag{13}$$

where D is the dissipation rate per unit undeformed volume; $\boldsymbol{P}$ is the first Piola-Kirchhoff stress; s is the entropy per unit undeformed volume. Inserting the explicit expressions for the terms in Helmholtz free energy Eq. (6), (11), (12) into Eq. (13) and assuming that D is independent of $\dot{\boldsymbol{F}}_e^T$ and $\dot{\theta}$, results in the elasticity law as well as the expression for the entropy

$$\boldsymbol{P} = J_t \frac{\partial \psi^e}{\partial \boldsymbol{F}_e} \cdot \boldsymbol{F}_t^{-1} = J_t \boldsymbol{F}_e \cdot \frac{\partial \psi^e}{\partial \boldsymbol{E}_e} \cdot \boldsymbol{F}_t^{-1}; \qquad \boldsymbol{\sigma} = J^{-1} \boldsymbol{P} \cdot \boldsymbol{F}^T = J_e^{-1} \boldsymbol{F}_e \cdot \frac{\partial \psi^e}{\partial \boldsymbol{E}_e} \cdot \boldsymbol{F}_e^T; \tag{14}$$

$$s = -\frac{\partial \psi}{\partial \theta}, \tag{15}$$

where $\boldsymbol{\sigma}$ is the Cauchy stress. Let $\dot{c}_{ij}$ be the rate of change of the volume fraction c_i due to a phase transformation $j \to i$. Then

$$\dot{c}_i = \sum_{j=0}^{m} \dot{c}_{ij}, \quad \dot{c}_{ij} = -\dot{c}_{ji}, \quad \dot{c}_{ii} = 0, \quad (i = 1, 2, \ldots, m, \quad j = 0, 1, \ldots, m). \tag{16}$$

Taking into account these relationships and $c_0 = 1 - \sum_{i=1}^{m} c_i$, the dissipation rate reduces to

$$D = \sum_{i=1}^{m} X_{i0}\dot{c}_{i0} + \sum_{j=1}^{m-1}\sum_{i=j+1}^{m} X_{ij}\dot{c}_{ij} \geq 0;$$

$$X_{i0} = W_{i0} - \frac{J_t}{2}\boldsymbol{E}_e\!:\!(\boldsymbol{C}_i - \boldsymbol{C}_0)\!:\!\boldsymbol{E}_e - \frac{J_t}{2}(\boldsymbol{E}_e\!:\!\boldsymbol{C}(c)\!:\!\boldsymbol{E}_e)\boldsymbol{F}_t^{-1}\!:\!\boldsymbol{\varepsilon}_{ti} - \Delta\psi^{\theta} - \mathcal{A}(1-2c) - 2\sum_{k=1}^{m}\mathcal{A}_{ik}c_k;$$

$$X_{ij} = W_{ij} - \frac{J_t}{2}\boldsymbol{E}_e\!:\!(\boldsymbol{C}_i - \boldsymbol{C}_j)\!:\!\boldsymbol{E}_e - \frac{J_t}{2}(\boldsymbol{E}_e\!:\!\boldsymbol{C}(c)\!:\!\boldsymbol{E}_e)\boldsymbol{F}_t^{-1}\!:\!(\boldsymbol{\varepsilon}_{ti} - \boldsymbol{\varepsilon}_{tj}) - 2\sum_{k=1}^{m}(\mathcal{A}_{ik} - \mathcal{A}_{jk})c_k;$$

$$W_{i0} = \boldsymbol{P}^T\!\cdot\!\boldsymbol{F}_e\!:\!\boldsymbol{\varepsilon}_{ti} = J\boldsymbol{F}_e^{t}\!\cdot\!\boldsymbol{\sigma}\cdot\boldsymbol{F}_e^{t-1}\cdot\boldsymbol{F}_t^{-1}\!:\!\boldsymbol{\varepsilon}_{ti}; \quad W_{ij} = \boldsymbol{P}^T\!\cdot\!\boldsymbol{F}_e\!:\!(\boldsymbol{\varepsilon}_{ti} - \boldsymbol{\varepsilon}_{tj}) = J\boldsymbol{F}_e^{t}\!\cdot\!\boldsymbol{\sigma}\cdot\boldsymbol{F}_e^{t-1}\cdot\boldsymbol{F}_t^{-1}\!:\!(\boldsymbol{\varepsilon}_{ti} - \boldsymbol{\varepsilon}_{tj}). \tag{17}$$

Here W_{i0} and W_{ij} are the transformation works for $A \to M_i$ and $M_j \to M_i$ PTs, respectively, and $\Delta\psi^{\theta} = \psi_M^{\theta} - \psi_0^{\theta}$. The first term in Eq. (17)$_1$ represents the dissipation rate due to the austenite to martensite PT and the second term represents the PT between martensitic variants. The third terms in expressions for X_{i0} and X_{ij} come from the differentiation

$$\frac{\partial J_t}{\partial c_i} = J_t\boldsymbol{F}_t^{-1}\!:\!\frac{\partial \boldsymbol{F}_t}{\partial c_i} = J_t\boldsymbol{F}_t^{-1}\!:\!\boldsymbol{\varepsilon}_{ti}. \tag{18}$$

The corresponding driving forces X_{i0} and X_{ij} are positive for $A \to M_i$ and $M_j \to M_i$ PTs and negative for opposite transformations. Since we do not want to resolve interfaces between martensitic variants, we impose $\mathcal{A}_{ik} = 0$.

2.3. Kinetic equations and phase transformation criteria

One can use extremum principles of nonequilibrium thermodynamics e.g., by Onsager for linear relationship between the fluxes $\dot{c}_{ij}$ and the work-conjugate thermodynamic forces X_{ij}, Ziegler extremum principles for nonlinear system (Ziegler, 1977) or postulate of realizability (Levitas, 1995a; 1995b). However, we cannot justify and quantify the cross-effects, and we will neglect them, then there is no need for extremum principles. The kinetic equations and phase transformation criteria for the change of volume fractions are expressed for two different models. First, if we do not consider any athermal thresholds for the driving forces X_{i0} and X_{ij}, the linear kinetic equation and PT criteria can be written as

$$\begin{cases} \dot{c}_{ij} = \lambda_{ij}X_{ij} & \text{if} \quad \{X_{ij} > 0 \;\&\; c_i < 1 \;\&\; c_j > 0\} \quad j \to i \\ & \text{or} \quad \{X_{ij} < 0 \;\&\; c_i > 0 \;\&\; c_j < 1\} \quad i \to j \\ \dot{c}_{ij} = 0 & \text{otherwise;} \qquad\qquad\qquad\quad i, j = 0, 1, 2, \ldots, m, \end{cases} \tag{19}$$

where λ_{ij} are kinetic coefficients. Second, if we include a threshold for the driving forces (similar to the dry friction force or the yield strength), k_{i-0} for $A \leftrightarrow M_i$ PTs and k_{ij} for $M_j \leftrightarrow M_i$ PTs, more general kinetic equations can be presented. Thus, for the $A \leftrightarrow M_i$ PTs

$$\begin{cases} \dot{c}_{i0} = \lambda_{i0}(X_{i0} - k_{i-0}) & \text{if} \quad \{X_{i0} - k_{i-0}(c_i, \sigma_i) > 0 \;\&\; c_i < 1 \;\&\; c_0 > 0\} \quad A \to M_i \\ \dot{c}_{i0} = \lambda_{i0}(X_{i0} + k_{i-0}) & \text{if} \quad \{X_{i0} + k_{i-0}(c_i, \sigma_i) < 0 \;\&\; c_i > 0 \;\&\; c_0 < 1\} \quad M_i \to A \\ \dot{c}_{i0} = 0 & \text{otherwise;} \qquad\qquad\qquad\qquad\qquad\quad i = 1, 2, \ldots, m, \end{cases} \tag{20}$$

and for $Mj \leftrightarrow M_i$ PTs

$$\begin{cases} \dot{c}_{ij} = \lambda_{ij}sign(X_{ij})(|X_{ij}| - k_{ij}) & \text{if} \quad \{|X_{ij}| - k_{ij} > 0 \;\&\; c_i < 1 \;\&\; c_j > 0\} \quad M_j \to M_i \\ & \text{or} \quad \{|X_{ij}| - k_{ij} > 0 \;\&\; c_i > 0 \;\&\; c_j < 1\} \quad M_i \to M_j \\ \dot{c}_{ij} = 0 & \text{otherwise;} \qquad\qquad\qquad\qquad\quad i, j = 1, 2, \ldots, m. \end{cases} \tag{21}$$

Note that the non-strict inequalities for the volume fraction of phases in Eqs. (19)-(21) (which were used in Idesman et al. (2005)) mean that the PT from any phase does not occur if the parent phase does not exist and that the PT to any phase does not occur if the product phase is complete. This constraint allows one to satisfy one of the requirement of the theory for PTs in multiphase materials, namely that theory for m-phase materials reduces to the theory for $(m-1)$-phase material when the volume fraction of one of the phase is getting zero, see Tóth et al. (2015). Similar conditions were imposed in the phase-field approach to the grain growth in Kim et al. (2006).

Since we will show below that k_{i-0} may be negative, i.e., it can not only suppress but also promote PT, the athermal threshold term will be substituted with the effective threshold.

3. Stress- and volume fraction-dependent effective threshold

According to kinetic Eqs. (19) without effective thresholds, one can define condition $X_{ij} = 0$ as the thermodynamic equilibrium conditions in the sense that it leads to $\dot{c}_{ij} = 0$. Expressions for X_{ij} depend on the chosen dependencies of all material parameters of the mixture on c_i. For example, if instead of Eq. (2) one accepts a similar mixture rule for logarithm $\ln\boldsymbol{F}_t = \sum_{i=1}^{m}\ln\boldsymbol{F}_{ti}c_i$ (see Babaei and Levitas (2019); Basak and Levitas (2017, 2018); Levitas (2018); Tuma and Stupkiewicz (2016); Tuma et al. (2016)), the expression for X_{ij}, and the thermodynamic equilibrium conditions $X_{ij} = 0$ differ from

those accepted here. Due to energy barrier terms scaled with $\mathcal{A}$ and $\mathcal{A}_{ik}$, as well as the geometrically nonlinear contribution from $\boldsymbol{F}_t^{-1}(c_i)$ in expression for the transformation work W_{i0}, the thermodynamic equilibrium conditions depend on c_i. The thermodynamic equilibrium conditions $X_{ij}=0$ are not directly related to the equilibrium condition of equal Gibbs energy for complete phases, which is often used, e.g., in high-pressure research. Generally, strict thermodynamic equilibrium conditions can only be defined for phase interfaces, and they depend on the interface orientation (Grinfeld, 1991)). As we will see in Section 6.5, a phase equilibrium condition involving X_{i0} is meet on the majority of A-M interfaces, which confirms that our definition of X_{i0} is correct.

It is customary to describe the PT hysteresis and athermal dissipation, positive athermal thresholds (interface friction), and kinetic equations of the type of Eqs. (20) and (21) are introduced. Usually, the athermal thresholds for direct and reverse PTs are the same and are in most cases, constant. However, in some cases, the dependence of k_{i-0} on the volume fraction of martensite c was introduced, see, e.g., Levitas (1994).

Our goal here is to develop a general theory, which is applicable to cubic to tetragonal Si I↔Si II PTs in particular. The PT criteria for Si I↔Si II PT in a perfect crystal were found with the help of molecular dynamics simulations in Levitas et al. (2017a,b). These criteria are linear functions of the Cauchy stress components normal to the cubic faces of Si I, σ_i, and are weakly dependent on the shear stresses, see Fig. 1. The main problem is that these lines are not parallel and intersect at some point. After the intersection of these lines, they coincide. It is shown schematically in Fig. 1 that they also coincide with the conceptual phase equilibrium line. However, this was not checked, and generally, as we have mentioned above, the phase equilibrium line is not conceptually well defined because the equilibrium of phases depends on the orientation of a phase interface. A new nanoscale PFA was developed in Levitas (2018) that satisfies the PT criteria obtained by atomistic simulations. This was, in particular, achieved by introducing new interpolation functions of the order parameter η for the transformation strain tensor, different for each independent component. The evolution equation for η is $\dot{\eta}=LX_\eta$, where X_η is the local thermodynamic driving force for changing η. While the local thermodynamic equilibrium condition, $X_\eta=0$ depend on η, PT criteria are defined by the lattice instability conditions, $\partial X_\eta/\partial\eta|_{\eta=0}>0$ for A → M PT and $\partial X_\eta/\partial\eta|_{\eta=1}>0$ for M → A PT. Thus, nanoscale PT criteria are not directly related to X_η and the local thermodynamic equilibrium condition $X_\eta=0$.

It is clear that for real defective crystals, the PT criteria will be different, but defects cannot make PT lines parallel in the stress space. Indeed, single dislocation slightly changes the PT conditions under uniaxial compression but did not change the coinciding portion of PT lines; see Babaei and Levitas (2019). Thus, for our scale-free theory for real (defective) materials, we have to assume the experimentally determined PT conditions for the variant 1 with compressive transformation strain along direction 3 and equal transformation strains along directions 1 and 2 as

$$\begin{aligned} &A\to M_i: && a^d(\sigma_1+\sigma_2)+b^d\sigma_3>c^d;\\ &M_i\to A: && a^r(\sigma_1+\sigma_2)+b^r\sigma_3<c^r, \end{aligned} \tag{22}$$

where a^d, b^d, c^d, a^r, b^r and c^r are empirically determined constants. The equivalence of directions 1 and 2 for cubic to tetragonal PTs is taken into account.

Since we use the simple mixture theory with linear Eq. (2) for the transformation strain tensor, we cannot reproduce conditions (22) by changing interpolation functions for $\boldsymbol{F}_t$, similar to the nanoscale model in Levitas (2018). The only way to make our thermodynamic PT conditions (20) consistent with experimental conditions (22) is to assume that the effective thresholds k_{0i} and k_{i0} for direct and reverse PTs depend on σ_i. Note that for M_i↔M_j PTs, such a problem does not exist, and we can use constant $k_{ij}=k_{ji}$. Instead of using two different k_{i0} and k_{0i}, we will use volume fraction dependent $k_{i-0}(c,\sigma_i)$, which gives $k_{i0}=k_{i-0}(0,\sigma_i)$ for $A\to M$ PT and $k_{0i}=k_{i-0}(1,\sigma_i)$ for $M\to A$ PT.

In order to reproduce the linear in stress PT conditions (22) obtained in experiments, we accept

$$k_{i-0}=J[a_1(c_i)(\sigma_1+\sigma_2)+a_3(c_i)\sigma_3];\qquad a_k(c_i)=d_k+(r_k-d_k)c_i;\quad (k=1 \text{ and } 3). \tag{23}$$

d_k and r_k are the fitting parameters, which can be calibrated by equaling our PT criteria with the PT conditions (22) obtained by experiments. The Jacobian J is included to compensate Jacobian in the transformation work W_{i0}.

The explicit expressions for PT conditions for the onset of direct $A\to M_i$ and reverse $M_i\to A$ PTs can be obtained from inequalities in Eq. (20) $X_{i0}-k_{i-0}>0$ at $c_i=0$ and $X_{i0}+k_{i-0}>0$ at $c_i=1$, respectively. Since PT criteria are linear in the Cauchy stresses, nonlinear terms with elastic energy are small in comparison with other terms, and can be neglected for calibration. Since experimental criteria (22) are expressed in terms of normal to the cubic faces Cauchy stresses σ_i, we also will consider loading by the normal stresses σ_i only. For such a loading, tensors $\boldsymbol{\sigma}$, $\boldsymbol{F}_e$, $\boldsymbol{F}_t$, and $\boldsymbol{\varepsilon}_t$ are coaxial and can be permuted in the scalar product. Thus, $\boldsymbol{F}_e^T\cdot\boldsymbol{\sigma}\cdot\boldsymbol{F}_e^{T-1}=\boldsymbol{\sigma}\cdot\boldsymbol{F}_e^{T-1}\cdot\boldsymbol{F}_e^T=\boldsymbol{\sigma}$, and $W_{i0}=J\boldsymbol{\sigma}\cdot\boldsymbol{F}_t^{-1}:\boldsymbol{\varepsilon}_{ti}$. Then we can express the PT conditions for direct and reverse PTs between austenite and martensite as

$$\begin{aligned} &A\to M_i: X_{i0}-k_{i-0}|_{c_i=0}>0 \;\Rightarrow\; (\sigma_1+\sigma_2)(\varepsilon_{t1}-d_1)+\sigma_3(\varepsilon_{t3}-d_3)>\frac{1}{J|_{c_i=0}}(\Delta\psi^\theta+\mathcal{A});\\ &M_i\to A: X_{i0}+k_{i-0}|_{c_i=1}<0 \;\Rightarrow\; (\sigma_1+\sigma_2)\Big(\frac{\varepsilon_{t1}}{1+\varepsilon_{t1}}+r_1\Big)+\sigma_3\Big(\frac{\varepsilon_{t3}}{1+\varepsilon_{t3}}+r_3\Big)<\frac{1}{J|_{c_i=1}}(\Delta\psi^\theta-\mathcal{A}). \end{aligned} \tag{24}$$

Table 1
Material parameters including kinetic coefficient $\lambda\,(\mathrm{Pa}\cdot\mathrm{s})^{-1}$, dimensionless constants in the expression for effective thresholds, as well as interaction coefficient A, jump in the thermal energy $\Delta\psi^{\theta}$, and elastic constants, all in GPa.

λ	A	$\Delta\psi^{\theta}$	d_1	d_3	r_1	r_3		
0.02	2	2.47	0.082	0.111	-0.90	0.338		
C_0^{11}	C_0^{44}	C_0^{12}	C_1^{11}	C_1^{33}	C_1^{44}	C_1^{66}	C_1^{12}	C_1^{13}
167.5	80.1	65.0	174.76	136.68	60.24	42.22	102.0	68.0

By equaling Eqs. (24) and (22), the fitting parameters d_1, d_3, r_1 and r_3 in the effective threshold can be calibrated from the following system of linear equations:

$$\frac{\varepsilon_{t1}-d_1}{\varepsilon_{t3}-d_3}=a^d;\quad \frac{\frac{\varepsilon_{t1}}{1+\varepsilon_{t1}}+r_1}{\frac{\varepsilon_{t3}}{1+\varepsilon_{t3}}+r_3}=a^r;\quad \frac{\Delta\psi^{\theta}+A}{J|_{c_i=0}(\varepsilon_{t3}-d_3)}=c^d;\quad \frac{\Delta\psi^{\theta}-A}{J|_{c_i=1}(\frac{\varepsilon_{t3}}{1+\varepsilon_{t3}}+r_3)}=c^r. \tag{25}$$

4. Material parameters and calibration of phase transformation criteria

The material parameters used in this paper are listed in Table 1. The transformation strain for Si I → Si II obtained in MD simulations (Levitas et al., 2017a; 2017b)) is $\varepsilon_t=(0.1753;\,1753;\,-0.447)$, which is large. The kinetic coefficient λ and interaction parameter A are chosen in a way that the rate of transformation is comparable with strain rate, and localization of strain is ensured. Jump in the thermal energy $\Delta\psi^{\theta}$ can be estimated from the thermodynamic equilibrium equation under hydrostatic condition. Thus, neglecting elastic strain and change in elastic moduli during PT, we obtain $\sigma_0^{eq}(\bar{J}_t-1)=\Delta\psi^{\theta}(\theta)$, where $\bar{J}_t=J_t$ at $c=1$. Under quasi-hydrostatic conditions, phase equilibrium mean stress σ_0^{eq} for PTs Si I↔Si II at room temperature is -10.5 GPa (Voronin et al., 2003) and $\bar{J}_t=0.764$. The elastic constants are known for Si and are taken from Chen et al. (2020); Schall et al. (2008).

From many experimental results for Si I → Si II PT under hydrostatic loading, it can be accepted that the PT pressure $p=-1/3(\sigma_1+\sigma_2+\sigma_3)$ for the appearance of Si II is in the range 11.3–12.5 GPa (Domnich et al., 2004). However, the transition pressure is lowered by the application of non-hydrostatic stress. For the sample within a gasket without a pressure-transmitting medium a transition pressure onset of ~ 8.5 GPa was reported in Hu et al. (1986) and ~ 8.3 GPa for 100 nm particles in Zeng et al., 2020). This was in good accordance with the results of Gupta and Ruoff (1980) who found an initial drop in resistance at ~ 8 GPa when uniaxial stress was applied along the [111] direction. Therefore, having two points, $\sigma_3=-8$ GPa for uniaxial compression and $p=12$ GPa for hydrostatic loading for the Si I → Si II PT, we can define the direct PT line as $1/6(\sigma_1+\sigma_2)-\sigma_3>8$ (GPa) (Fig. 2).

However, reverse Si II → Si I PT has not been observed in experiments. Instead, Si II transforms to other phases such as Si III or Si XII during releasing the applied stress (Domnich et al., 2004), which we will not consider here. Therefore, there is no reliable information to be used for the calibration of the reverse instability line. In first principle simulations for an ideal crystal (Zarkevich et al., 2018), lattice instability stress for reverse PT in uniaxial loading is tensile, however, defects may increase this stress. Thus, making an assumption, we consider the Si II → Si I instability line as $1/8(\sigma_1+\sigma_2)-\sigma_3>1$ which assumes instability point as $\sigma_3=-1$ GPa and $p=4/3$ GPa for uniaxial compression and hydrostatic conditions, respectively. Considering the two mentioned direct and reverse instability lines, we can calibrate PT conditions for our model using Eq. (25), and obtain the effective threshold fitting parameters d_1, d_3, r_1 and r_3 in Table 1.

Relative positions of the lines for initiation of the direct and reverse PTs as well as phase equilibrium lines $X_{i0}=0$ (i.e., for $k_{i-0}=0$, like in classical thermodynamics) for $c=0$ and $c=1$ are shown in Fig. 2. Since we did not plan to describe transformational behavior for coinciding lines for initiation of the direct and reverse PTs as it is done in Babaei and Levitas (2018, 2019) for a nanoscale model, and qualitatively new results are not expected, the intersection of the direct and reverse PT lines is shifted to large tensile stresses by selecting the corresponding reverse PT line. The slope of phase equilibrium lines is fully determined by the expression of transformation work $W_{i0}=J\boldsymbol{\sigma}\cdot\boldsymbol{F}_t^{-1}(c_i)\boldsymbol{:\varepsilon}_{ti}$, which does not have free fitting parameters. Due to geometrically nonlinear term $\boldsymbol{F}_t^{-1}(c_i)$, the slope of phase equilibrium lines depends on c_i and is very different for $c_i=0$ and $c_i=1$. We will focus on the $A\rightarrow M_i$ PT. It is clear from Fig. 2 that the phase equilibrium line for $c_i=0$ and $A\rightarrow M$ PT line intersect at $\sigma_1=-12.97$ GPa, and for larger compressive stresses, PT condition is satisfied for $X_{i0}<0$, which leads to the negative dissipation rate $X_{i0}\dot{c}_i$. This formal violation of the second law of thermodynamics requires special discussion.

Change in PT stresses within experimental scatter from different sources can slightly change the slope of the PT line and shift intersection point to higher stresses σ_1 but cannot eliminate intersection and formal violation of the second law of thermodynamics. The phase equilibrium line can potentially be changed if we include a change in the second- and higher-order elastic constants in X_{i0}, i.e., include a jump in elastic strains. However, these nonlinear terms are either small (because elastic strains are much smaller than the transformation strains) or they will change PT conditions to the nonlinear conditions with a similar trend as for phase equilibrium conditions. Since the bulk modulus for Si-I and Si-II are $K_0=99.16$

GPa and $K_1 = 106.91$ GPa, respectively (calculated based on the C^{ij} (Lekhnitskii, 1963)), the jump in the volumetric elastic strain under hydrostatic loading and phase equilibrium pressure 12 GPa is 0.008, which is much smaller than the jump in transformation volumetric strain $|J_t - 1| = 0.236$.

As we discussed, the phase equilibrium conditions $X_{i0} = 0$ under general stress tensor do not have a lot of physical sense because actual phase equilibrium conditions are defined at interfaces and depend on the orientation of the interfaces. Even for the hydrostatic loading, $\boldsymbol{\sigma} = \sigma_0 \boldsymbol{I}$, the transformation work

$$W_{i0} = J\boldsymbol{\sigma} \cdot \boldsymbol{F}_t^{-1}(c_i) : \boldsymbol{\varepsilon}_{ti} = J\sigma_0 \boldsymbol{F}_t^{-1}(c_i) : \boldsymbol{\varepsilon}_{ti} \tag{26}$$

is different from the correct expression $\sigma_0(J_t - 1)$ for neglected elastic strains. This correct expression can be obtained using

$$W_{i0} = J\boldsymbol{\sigma} \cdot \boldsymbol{F}_t^{-1} : \frac{d\boldsymbol{F}_t}{dc_i} \simeq J_t \sigma_0 \boldsymbol{F}_t^{-1} : \frac{d\boldsymbol{F}_t}{dc_i} = \sigma_0 \frac{dJ_t}{dc_i} \tag{27}$$

(Eq. (18) was utilized) and $\bar{J}_t = 1 + (\bar{J}_t - 1)c$. However, this kinematic equation does not correspond to the traditional mixture rule (2).

From the other side, there are well-documented experimental results showing that under plastic straining PT may occur at a pressure much below than the phase equilibrium pressure. Thus, the phase equilibrium pressure is estimated as 10.5 GPa for Si I -Si II (Voronin et al., 2003) and is in the same range for Si I -Si III (Blank and Estrin, 2013). Under large plastic shear, PT Si I → Si III occurs at 2.7 GPa and PT Si I → Si II (via Si III) occurs at 5.4 GPa. Similarly for Ge, phase equilibrium pressure (triple point) for Ge I- Ge II-Ge III is 9 GPa; under large plastic shear, PT Ge I → Ge III occurs at 3.3 GPa and PT Ge I → Ge II (via Ge III) occurs at 4.5 GPa (Blank and Estrin, 2013). More recent experiments exhibit PT from graphite to the hexagonal and cubic diamond at 0.4 and 0.7 GPa under shear, while phase equilibrium pressure is 2.45 GPa under hydrostatic conditions, 2.24 GPa under uniaxial compression, and 1.94 GPa under compression and shear (Gao et al., 2019). For $\alpha - \omega$ PT in Zr, phase equilibrium pressure is 3.4 GPa under hydrostatic conditions, while under shear, this PT was obtained at 1.2 GPa (Pandey and Levitas, 2020). Such a counterintuitive behavior was explained analytically in Levitas (2004) and within nano- and microscale PFA in Javanbakht and Levitas (2015, 2018), Levitas et al. (2018) and Esfahani et al. (2020) by strong stress tensor concentration produced by defects induced by plastic deformation, e.g., dislocation pileups. Consequently, while with dislocations in theory, this behavior was thermodynamically consistent, without defects, it leads to negative dissipation, as observed in our case.

Thus, the simplest way to resolve the behavior when the PT condition to a high-pressure phase is met at stresses lower than those defined by the phase equilibrium condition is to assume that k_{i-0} may be negative because of local stress concentrators and some conceptual indeterminacy in the phase equilibrium conditions $X_{i0} = 0$. Then, the theory is based on the experimentally calibrated PT conditions $X_{net} = X_{i0} - k_{i-0} > 0$ and kinetics in terms of the net driving force $X_{net} > 0$. Therefore, components of X_{net}, namely X_{i0} and k_{i-0} do not appear in theory separately. Note that the athermal threshold k_{i-0} in traditional theories is caused by the Peierls barrier and interaction between interfaces and stress fields of defects, e.g., point defects and dislocation forest (Ghosh and Olson, 1994a, 1994b; Grujicic et al., 1985). Thus, the only difference with the traditional approach is that we included in k_{i-0}, not only contributions that suppress the PT, but also those which promote PT, similar to the PFA in Javanbakht and Levitas (2015, 2018), Levitas et al. (2018) and Esfahani et al. (2020).

5. Problem formulation and solution for multivariant microstructure evolution

Finite Element Method (FEM) algorithm and computational procedures are developed in the open-source FEM code deal.II (Bangerth et al., 2007). 3D cubic linear elements (8 nodes) with first-order interpolation and full integration are considered. Computational challenges are related to large complete transformation strains (−0.447) because transformation strain varies from zero to its maximum magnitude within numerous phase interfaces with a width of a single finite element, which may cause divergence of the iterative solution process.

To study the microstructure evolution at the microscale, we solve a number of problems to model Si I↔Si II PTs. We consider a 3D parallelepiped sample of size $0.5 \times 1 \times 3$ in x, y, and z spatial directions, respectively (Fig. 3). We would like to mention that since the theory is scale-free, the dimensions of the sample do not have any length unit. However, from the formulation of the physical model, the dimensions should be larger than the micrometer. The effect of changing the sample size on the martensitic microstructure was studied in Esfahani et al. (2020) using a similar scale-free PFA but for small strain formulations and two dimensions. It was found that change in all sizes (keeping geometric similarity) by up to three orders of magnitude did not change microstructure and the entire solution. One of the external faces with a normal in x-direction is shear-stress-free and fixed for out-of-plane displacement to be a symmetry plane, and another face with a normal in x-direction is stress-free. Two external faces with a normal in y-direction are stress-free. One external face with a normal in z-direction has zero displacements in all directions and another face is fixed for in-plane displacements and is under compressive constant, growing in time displacement u in z-direction. Two types of loadings are considered:

- With the prescribed constant macroscopic rate of the Lagrangian strain, $\dot{E}$, in z-direction, determined in terms of displacement u and sample lengths.
- Quasi-static loading: constant displacement increments Δu are applied with some holding time t_h between each increment for relaxation of stresses and letting microstructure move toward the stationary solution for each Δu.

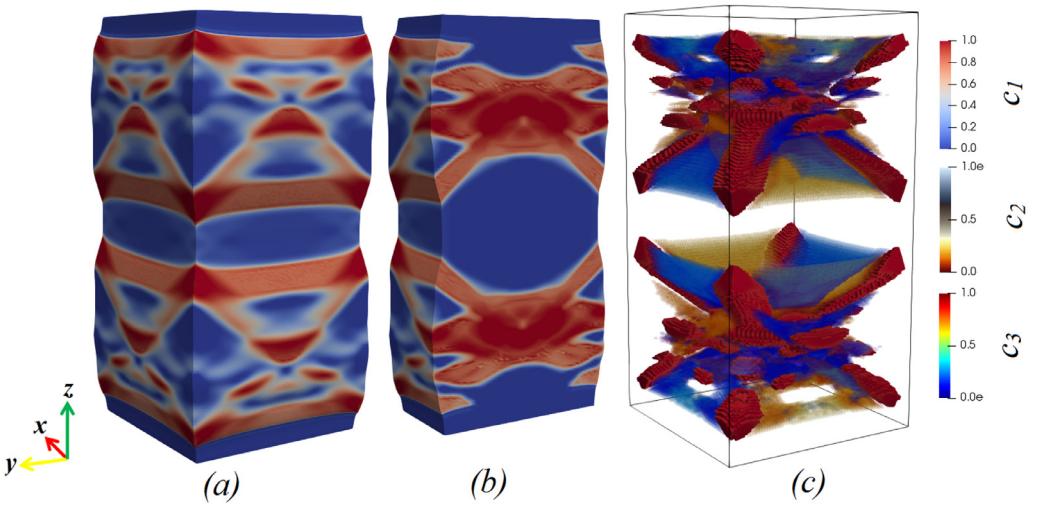

Fig. 3. Microstructure during Si I↔Si II PTs for quasi-static loading for $\Delta u = 0.0075$ and $t_h = 10\ s$ and $E = 0.096$. (a) the Volume fraction of the variant M_1, external view of the entire sample; (b) the volume fraction of the variant M_1, internal view on the half of the sample, and (c) the transparent view showing all martensitic variants excluding austenitic regions. The regions, which are completely transformed to the dominant first variant ($c_1 = 1$, red color), as well as the regions which are partially transformed to the second (yellow color) and third (blue color) variants with the maximum volume fraction $c_2 = c_3 = 0.3$ are shown. (For interpretation of the references to color in this figure legend, the reader is referred to the web version of this article.)

The samples with three different representations of the solution fields for the volume fraction of phases used in this paper are shown in Fig. 3 for $\Delta u = 0.0075$ and $t_h = 10\ s$ and $E = 0.096$.

(a) We reflect the simulation fields with respect to the symmetry plane and obtain the entire sample of size $1 \times 1 \times 3$, whose external view is shown in Fig. 3(a).
(b) A view of the sample cut at the symmetry plane is shown in Fig. 3(b).
(c) A transparent view of the sample with all three martensitic variants is shown in Fig. 3(c), after excluding the austenitic regions.

Please refer to the supplementary materials where videos of the microstructure evolution process for the three mentioned perspectives in Fig. 3 are presented. The transparent view of the microstructure evolution during the PT is shown in Figs. 4 and 5 for applied quasi-static compressive loading with $\Delta u = 0.0075$ and $t_h = 10\ s$. While in Fig. 4, only the regions with the maximum volume fraction of the martensitic variants are shown, in Fig. 5, the distribution of volume fraction of each martensitic variant is presented separately. After macroscopic Cauchy stress (averaged over the top surface stress σ_z) reaches the PT stress 8 GPa and the clamped boundary conditions at the top and bottom faces create heterogeneous internal stresses, the first martensitic variant nucleates along the eight inclined Si II bands, branched from the external edges toward the symmetry axes z at both top and bottom of the sample. In addition, eight Si II bands initiate from the edges above and below the horizontal symmetry plane of the sample, and propagate to the symmetry axes z, approximately symmetric to the Si II regions propagating from the top and bottom surfaces with respect to horizontal planes. These branches continue to grow toward the center and meet there to form two internal regions of complete multivariant Si II. Besides, despite the external loading being favorable for the growth of the first variant, second and third variants are also growing on some inclined planes between the branches of the first variant to relax the internal stresses due to the first variant. The field for c_2 can be approximately obtained from the field of c_3 by rotation by 90^o with respect to z-axis. However, the volume fraction of the second and third variants is at most ~ 0.3 in these regions. The central region of the sample is initially untransformed. The combination of martensitic variants produces two curved bowl structures symmetric with respect to horizontal symmetry plane, which grow and get closer to each other with continuing loading, so that finally these structures coalesce and the middle of the sample completely transforms to the first variant. Consequently, variants M_2 and M_3 appear as the stress and elastic energy relaxation mechanism for the reduction of the internal stresses generated by $A \to M_1$ PT, which disappear throw $M_2 \to M_1$ and $M_3 \to M_1$ transformations at the end driven by the reduction of the internal stresses and interface energy of the variant-variant interfaces. Thus, in many regions, $A \to M_1$ PT is substituted with $A \to M_2 \to M_1$ and $A \to M_3 \to M_1$ PTs via incomplete variants M_2 and M_3, which are intermediate phases.

Alternative representations of the solution fields of all Si II variants, which include Si I regions during microstructure evolution as well, are shown in Fig. 6. The figure includes the internal view as well as the external view from the backside of a sample in Fig. 3. Similar to Figs. 3–5, the solution is approximately symmetric with respect to the horizontal symmetry plane of the sample. Except for the branches of completed variant M_1 depicted in the transparent view, in other Si II regions, all Si II variants occupy some portion of the volume. In other words, as can be seen in both the internal and external view of Fig. 6, there are regions within the intersecting bands of complete Si II with the variant M_1 in the range of $0.6 < c_1 < 1$

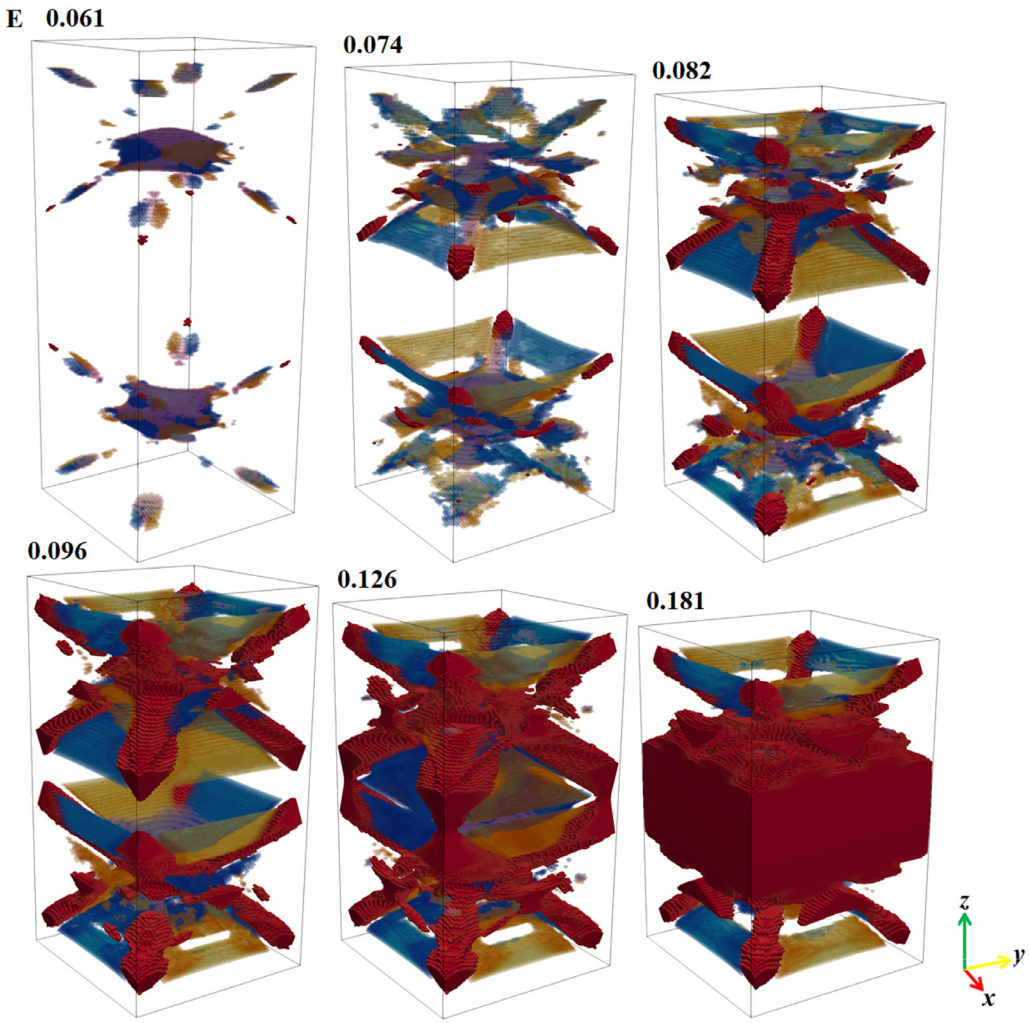

Fig. 4. Transparent view of microstructure evolution during Si I↔Si II PTs showing regions with the maximum value of all martensitic variants ($c_1 = 1$ and $c_2 = c_3 = 0.3$) for quasi-static compressive loading with $\Delta u = 0.0075$ and $t_h = 10$ s.

and the rest is occupied by the variants M_2 and M_3. In such a way, by internal twinning of Si II (which we do not resolve in our microscale treatment), the system reduces internal stresses. Note that twinned Si II was observed experimentally in Popov et al. (2015) during Si I → Si II PT under hydrostatic loading using Laue diffraction.

6. Effect of various parameters on microstructure evolution

6.1. Effect of the finite element size

The numerical solution for the materials, which exhibit material instability followed by strain-softening due to their constitutive equations, is mesh-size sensitive. Since we did not include gradient energy, a material does not have an energy-based internal size and does not preclude phase interface width from tending to zero. Still, theoretically, the problem is well-posed and strain-rate regularized due to kinetic Eq. (20). Indeed, if Si I-Si II interface width would tend to zero, $\dot{c}_{0i} \to \infty$, which requires infinite driving force X_{i0} and is impossible. However, when the system approaches a stationary microstructure, the rate-dependency weakens and disappears, and the interface width theoretically tends to zero. Then the interface width is limited by the size of a single finite element.

Therefore, we study the mesh sensitivity of our solutions to find conditions for which results are approximately independent of the mesh density. We consider four different mesh sizes for our sample with the same loading and boundary conditions explained before. While the initial width of the sample was chosen to be 1, the sizes of cubic elements in the reference configuration were accepted as 1/16, 1/32, 1/64, and 1/80 with a number of elements (NOE) equal to 6144, 49,152, 393,216, and 768,000 respectively.

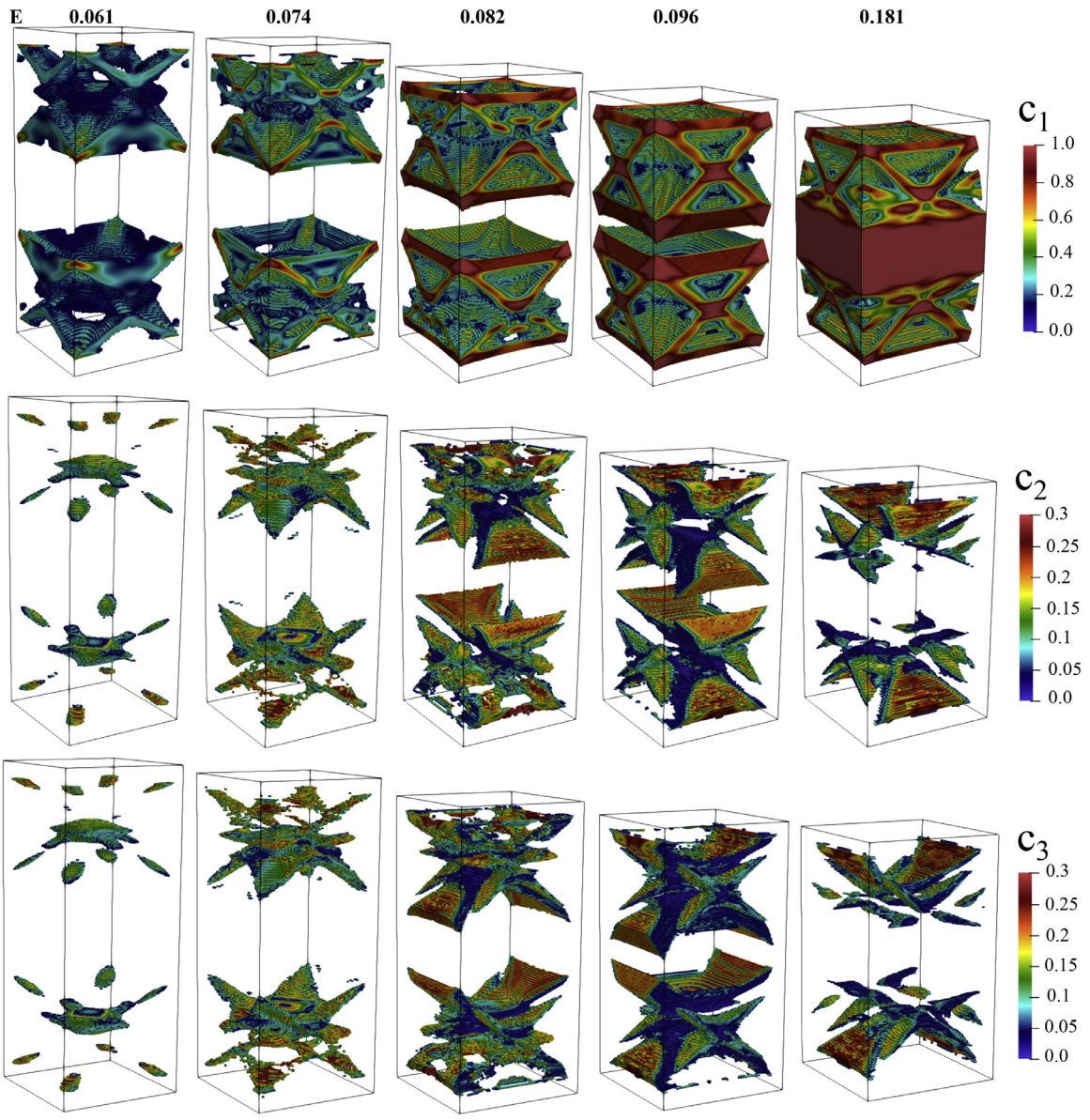

Fig. 5. Transparent view of microstructure evolution during Si I↔Si II PTs showing full distribution ($0 < c_1 \leq 1$ and $0 < c_2$ and $c_3 \leq 0.3$) of all martensitic variants separately for quasi-static compressive loading with $\Delta u = 0.0075$ and $t_h = 10\ s$.

The microstructure evolutions are shown in Fig. 7. To exclude the strain-rate dependency of the solution and to approach stationary solution during the evolution, we consider quasi-static loading with $\Delta u = 0.0075$ and $t_h = 10\ s$. It can be observed in Fig. 7 that for the first case with the coarse mesh and lowest number of elements (NOE=6144), the microstructure involves two main martensitic bands only approaching each other at the surface for both internal and external regions. While PT in the band is not completed, the diffuse interface is localized within one or two elements.

One step of refining the mesh (NOE=49152) leads to the formation of more complex and fine martensitic regions at the initial stages. However, with continued loading, the symmetry of solution with respect to vertical plane disappears, most of the martensitic regions coalesce and form two large Si II bands inside the sample, similar to those for NOE=6144, but fine microstructure still remains near the external faces. Thus, reverse PT in some regions occurs along with the direct PT under monotonous loading, despite the very large hysteresis introduced into the constitutive model.

For NOE=393216, a similar fine microstructure in initial stages is formed with even finer Si II regions, but it does not lose its symmetry with respect to the vertical plane and remains until the end of the loading. While lattice rotation in Si II is large, it is not visible in Si I. Further mesh refinement (NOE=768000) does not practically change the microstructure. This means that the result becomes practically mesh-independent when the ratio of the sample size to the element size

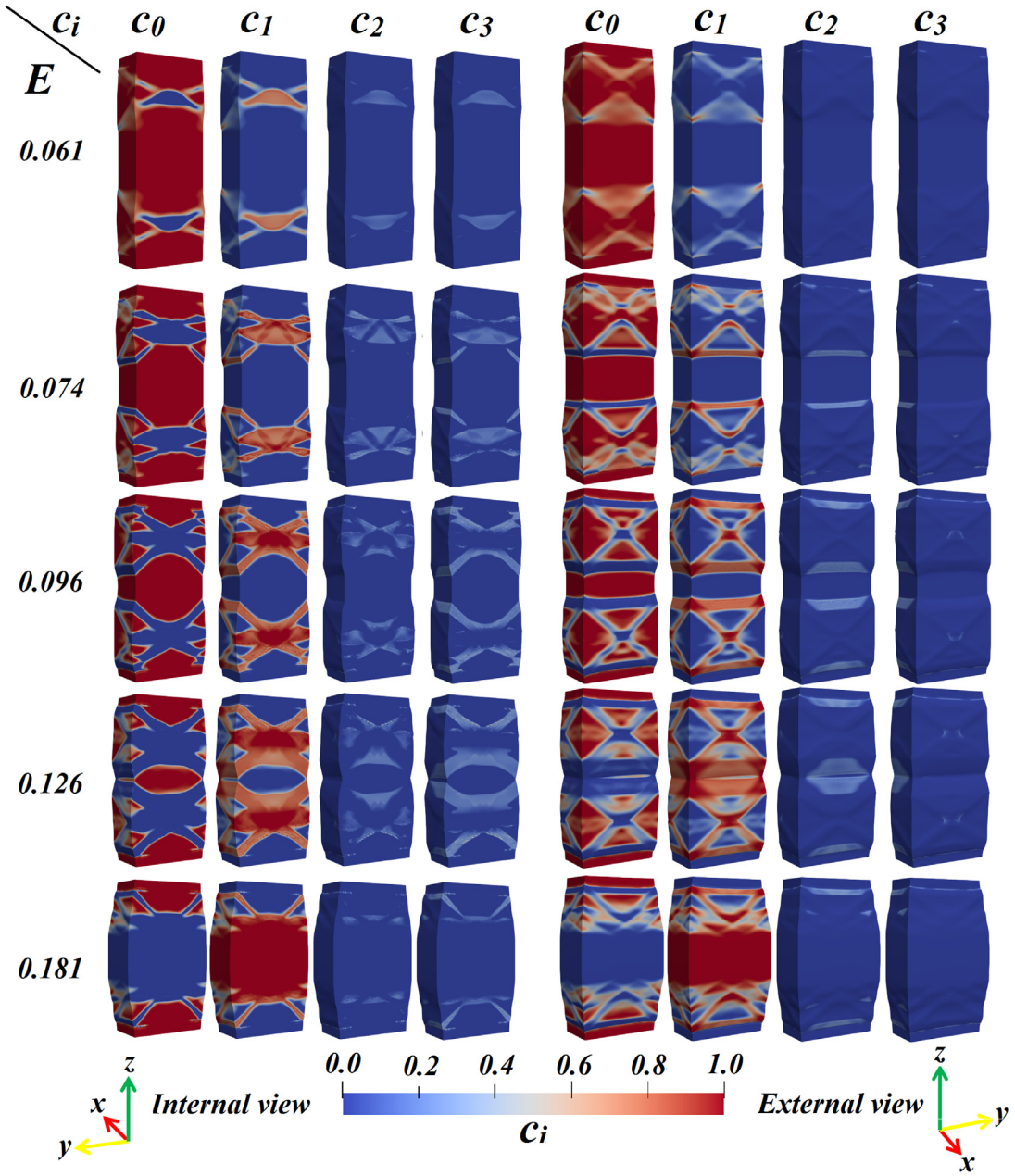

Fig. 6. Microstructure evolution during Si I → Si II PT under compression showing external (from the back side of sample in Fig. 3) and internal views of all martensitic variants for quasi-static compressive loading with $\Delta u = 0.0075$ and $t_h = 10\,s$.

exceeds 80. Note that practical mesh-independence for small-strain scale-free PFA was shown in Idesman et al. (2005) and Esfahani et al. (2018) for 2D problems. Only the interface width was different for different meshes, which did not affect the geometry of microstructure and macroscopic stress-strain curves. However, solutions contained only growing parallel bands, in contrast to 3D microstructure with complex geometry observed here.

6.2. Evolution of rotation of the crystal lattices of Si I and Si II

Deformed meshes in Figs. 7 and 8 clearly visualize large deformations and rotations of the initially cubic crystal lattice of Si I and tetragonal lattice of Si II. Thus, for NOE= 6144 and NOE=393216 in Fig. 7 and in many places in Fig. 8 rotations are (a) in the bulk Si I and Si II, they are different in different regions and may have even different signs; and (b) in Si I close to the diffuse interface. All rotations are driven by the minimization of the elastic energy generated by diffuse Si I-Si II

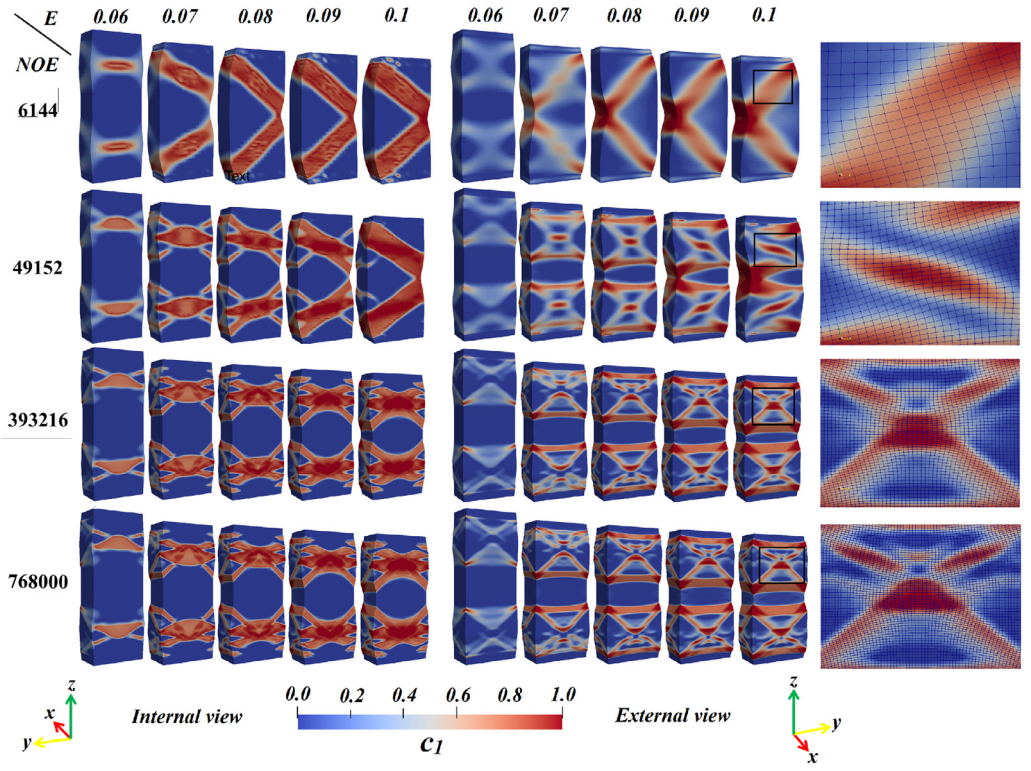

Fig. 7. Effect of element size on the microstructure evolution for quasi-static compressive loading with $\Delta u = 0.0075$ and $t_h = 10\ s$.

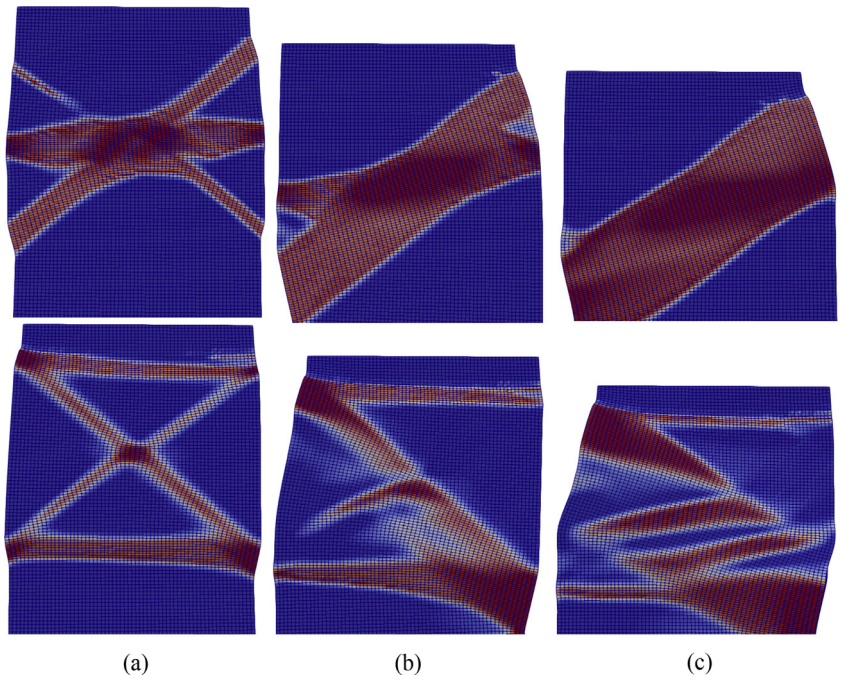

Fig. 8. Evolution of the rotation and deformation of the crystal lattices of Si I and Si II during a quasi-static loading with $\Delta u = 0.0075$ and $t_h = 10\ s$ at (a) $E = 0.08$; (b) $E = 0.09$; (c) $E = 0.01$; top row shows the internal view and the bottom row shows the external view. .

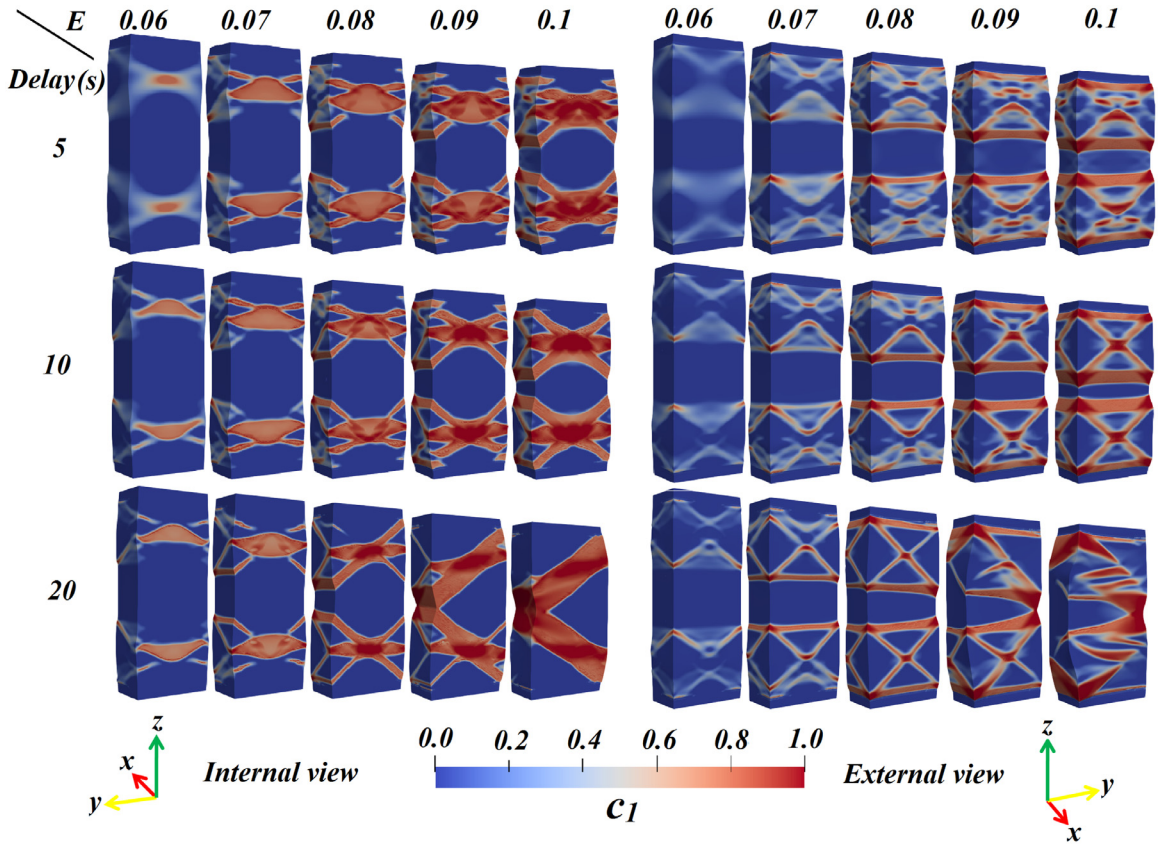

Fig. 9. Effect of different holding times (delays) for quasi-static loading on the microstructure evolution.

interfaces. Rotations of the lattice in Si II mean that despite the uniaxial compression along the cubic axis, which is perfectly aligned along the compressive transformation strain ε_{t3}, lattice rotates to reduce stresses at phase interfaces, leading to macroscopic transformation strain different from that for homogeneous transformation. In particular, the transformation strain in z-direction is smaller than ε_{t3}. This requires larger compressive stresses in z-direction for transformation. In many cases, lattice rotation in Si I and Si II regions correlate with a deviation of the free surface from the vertical direction. Heterogeneous rotations have two consequences:

- Our simulation reproduces the formation of diffuse grain boundary within Si I, which is getting polycrystalline. Lattice rotation in Si I during Si I to Si II PT was observed experimentally in Popov et al. (2015).
- Heterogeneity of lattice rotations in Si II in different regions explains "polycrystalline nature" of the Si II obtained from the single-crystal Si I in Popov et al. (2015).

In the regions where both cubic and tetragonal lattices are aligned along the interfaces (mostly horizontal and close to horizontal interfaces and Si II plates), due to coherence of the interfaces, the lattice of Si I is elastically expanded along the interface, which promotes PT. This extension reduces while moving from interfaces to the bulk Si I.

Note that after completion of PT, all rotations disappeared and homogeneous and perfectly aligned Si II single crystal is observed. This confirms that rotations are driven by misfit strain at the phase interfaces and represent a mechanism of elastic stress and energy relaxation additional to the appearance of the intermediate variants M_2 and M_3.

6.3. Effect of the holding time during the quasi-static loading

To study the microstructure evolution with a slow pace of loading and exclude the strain rate effect, we consider quasi-static loadings. We apply three different holding times t_h =5 s, 10 s, and 20 s, with fixed displacement increments $\Delta u = 0.0075$, so that the microstructure approaches closer to the stationary solution during the evolution process. In the internal view in Fig. 9 at the largest shown strain ($E = 0.1$) for the shortest holding time (5 s), the martensitic bands are separated from each other in some regions. Besides, the external view shows that there are regions of intermediate volume fraction of martensite around the completed regions. However, for the holding time of 10 s, the martensitic regions coalesce and form bands, and there are fewer regions transformed partially. Finally, for the holding time of 20 s, although for

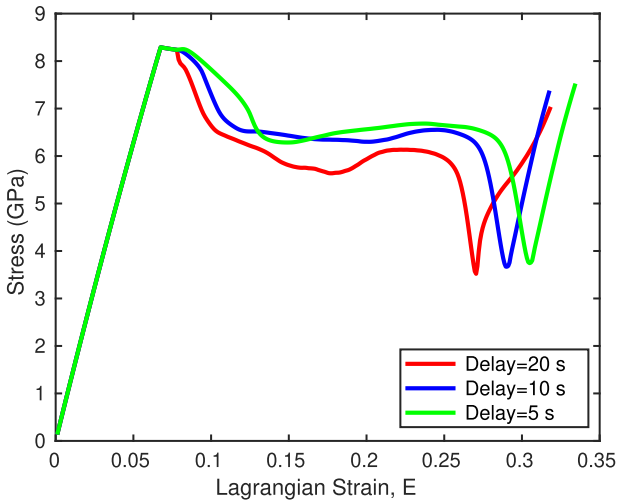

Fig. 10. The macroscopic Cauchy stress - Lagrangian strain curves for different holding times for a quasi-static loading.

$E \leq 0.07$ the microstructure is similar initially, for larger strains, symmetry with respect to the vertical plane and some of the martensitic bands disappear, and the morphology of microstructure completely changes from an intersection of multiple fine bands to only two main large bands inside the sample. A similar microstructure was obtained for rough meshes in Fig. 7. Nevertheless, the microstructure close to the external faces still remains multiconnected and nontrivial. It can be concluded that increasing holding time leads to a more completed PT and microstructure with fewer number of bands and interfaces (i.e., to coalescence) to minimize internal elastic-stress energy and interfacial energy. Based on the external view, even for 20 s, a stationary microstructure was not reached. By comparing Figs. 7 and 9, we also conclude that *for close to stationary microstructure, when fine features disappear, the roughest mesh gives the best solution in a more economical way.*

The macroscopic compressive stress-strain curves ($-\sigma_{33}$ versus E_{33}) for three holding times are presented in Fig. 10. At the very early stages of PT ($E_{33} < 0.07$) after PT onset at $\sigma_{33} = -8.2GPa$, the stress-strain curves coincide, as expected from similar initial microstructure for all cases. Later, longer holding time leads to lower internal stresses and total interfacial energy and more equilibrium microstructure, resulting in a decrease in stresses for the same strains. When microstructure from upper and lower parts of a sample coalesce, large increment in volume fraction c_1 and in corresponding transformation strain leads to a large decrease in the elastic strain and the Cauchy stress. The larger holding time is, the smaller is the prescribed strain at which such a coalescence occurs. This is related mostly to a larger amount of residual Si II near the top and bottom surfaces of the sample, especially for a two-band structure for $t_h = 20s$. After further loading, the nonlinear behavior of Si II for the longest holding time is caused by further PT progress and variant-variant transformation. For two other holding times, the behavior of Si II is practically linear elastic at least up to shown stresses. Different macroscopic transformation strains are related to the different amounts of residual Si I, mostly near the ends of a sample, due to different morphology of Si II regions.

6.4. Effect of strain rate

We consider three different strain rates, $\dot{E}$=0.002, 0.001, and 0.0005, and corresponding microstructure evolutions are shown in Fig. 11. It can be clearly seen that for the fastest loading ($\dot{E} = 0.002$) the sample involves some smeared microstructures with partially transformed regions in the major part of the sample, and the interface between totally transformed Si II and Si I is wide. For slower straining ($\dot{E} = 0.001$) the volume of the partially transformed regions reduces and the interface width shrinks. For the slowest strain rate ($\dot{E} = 0.0005$), with increasing strain, there are a very small number of regions with partial transformation, and the martensitic bands become fine and straight, with minimum interface width. The same reasoning as for quasi-static cases can be given here: as the pace of loading decreases, the transformative processes have more time to proceed and direct the system toward the minimum internal elastic and interfacial energy state.

The stress-strain curves for these strain rates are shown in Fig. 12. For small strains, after initiation of PT and during the softening regime, when stress drops from PT initiation stress (peak point) to the Maxwell stress modified by the effective threshold, the slower the loading, the lower the stress. This is expected because slower loading produces more Si I and, consequently, larger transformation strain. Thus elastic strain and stress relax more. With further straining, stress-strain curves exhibit the Maxwell stress plateau lifted up by the effective threshold, with practically the same stress for all strain rates. This means that for all strain rates, the growth rate of Si II is sufficient to support PT at stress close to that for the quasi-equilibrium loading. Small differences are caused by different microstructures for different strain rates. The difference in microstructure also determines different behavior during coalescence of Si II regions near the horizontal plane of the symmetry of a sample, which is nonmonotonous versus strain rate. For $\dot{E} = 0.0005$ and 0.002 1/s, stress-drop occurs in the

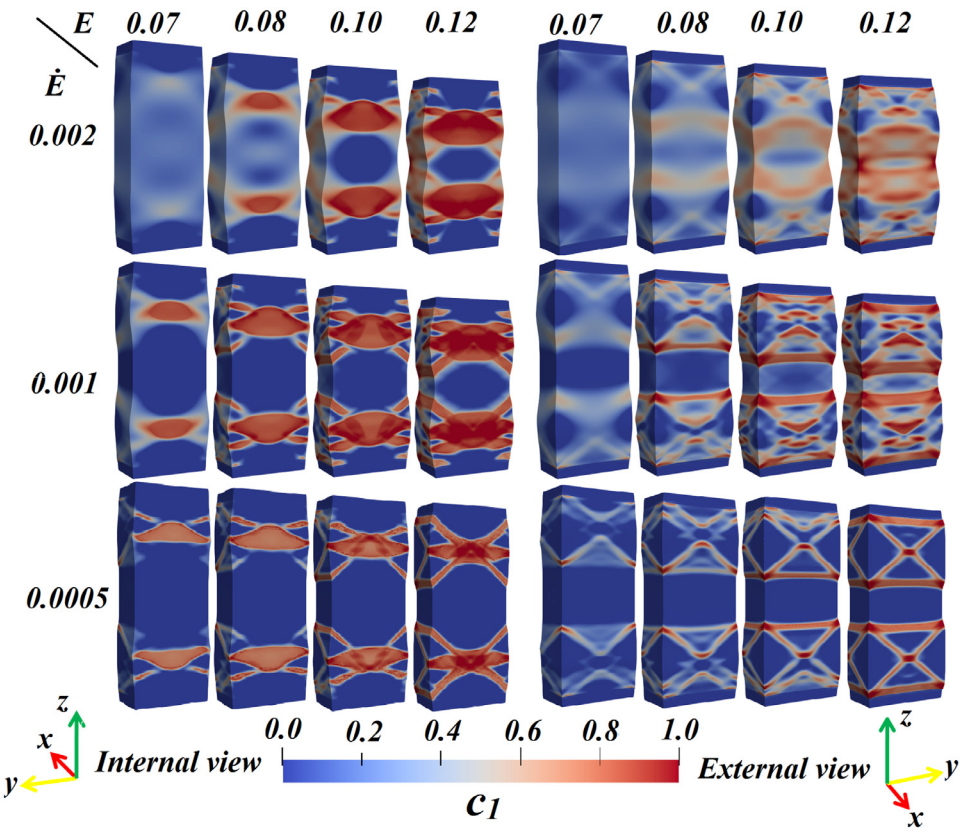

Fig. 11. Effect of the strain-rate on the microstructure evolution.

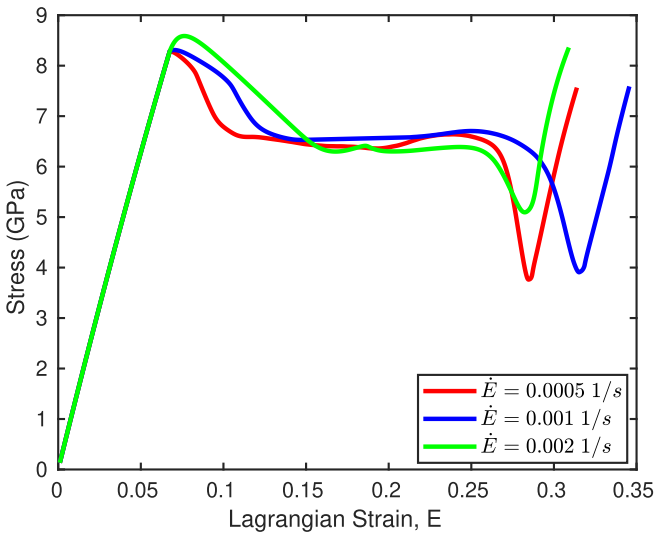

Fig. 12. Cauchy stress - Lagrangian strain curves for loadings with different strain-rates.

same strain range, but it is smaller for high strain rate due to smaller increments in the amount of Si II. For $\dot{E} = 0.001$ 1/s, stress drop starts approximately at the same strain, but it is spread over the larger strain interval due to different topology of the microstructure. After this, for two lower strain rates, loading lines are straight and parallel, hinting that there is no further PT to Si II. For the highest strain rate, the nonlinear stress-strain curve is related to some increase in the averaged volume fraction of Si II. Similar to Fig. 10, the difference in a macroscopic transformation strain is because of the different amount of residual Si I near the ends of a sample due to different morphology of Si II regions.

6.5. Phase equilibrium conditions at stationary austenite-martensite interfaces

The phase equilibrium condition for a sharp A-M interface with neglected surface energy is

$$X_\Sigma = \boldsymbol{P}^T\!:\!(\boldsymbol{F}_M - \boldsymbol{F}_A) - (\psi_M - \psi_A) = k_{A-M}, \tag{28}$$

where X_Σ is the Eshelby driving force for an interface propagation, subscripts A and M designate values in A and M, respectively, and k_{A-M} is the effective or athermal threshold for the A-M interface propagation. Using decomposition (1) and assuming small difference in $\boldsymbol{F}_e$ in A and M, we obtain $\boldsymbol{F}_M - \boldsymbol{F}_A = \boldsymbol{F}_e{\cdot}(\boldsymbol{F}_{tM} - I) = \boldsymbol{F}_e{\cdot}\boldsymbol{\varepsilon}_{tM}$ and

$$X_\Sigma = \boldsymbol{P}^T\!:\!\boldsymbol{F}_e\!:\!\boldsymbol{\varepsilon}_{tM} - (\psi_M - \psi_A) = k_{A-M}, \tag{29}$$

Note that using the mixture rules

$$\boldsymbol{F} = (1-c)\boldsymbol{F}_A + c\boldsymbol{F}_M; \qquad \psi = (1-c)\psi_A + c\psi_M, \tag{30}$$

substituting them in the dissipation inequality (13), and assuming that the A-M PT is the only dissipative process and isothermal conditions, we obtain

$$D = \left(\boldsymbol{P}^T\!:\!\frac{\partial \boldsymbol{F}}{\partial c} - \frac{\partial \psi}{\partial c}\right)\dot{c} = X_\Sigma \dot{c} \geq 0, \tag{31}$$

with X_Σ from Eq. (28). If instead of equation $\boldsymbol{F} = (1-c_M)\boldsymbol{F}_A + c_M\boldsymbol{F}_M$ we assume $\boldsymbol{F} = \boldsymbol{F}_e{\cdot}[(1-c_M)\boldsymbol{I} + c_M\boldsymbol{F}_{tM}]$, then we obtain Eq. (31) with X_Σ from Eq. (29).

To find expression for X_Σ in Eq. (29) in terms of X_{i0} from Eq. $(17)_1$, we note that using the mixture rules

$$\boldsymbol{F} = \boldsymbol{F}_e{\cdot}\left[\boldsymbol{I} + \sum_{i=1}^{m} c_i\boldsymbol{\varepsilon}_{ti}\right]; \qquad \psi = (1-c)\psi_A + c\psi_M = \left(1 - \sum_{i=1}^{m} c_i\right)\psi_A + \sum_{i=1}^{m} c_i\psi_M, \tag{32}$$

substituting them in the dissipation inequality (13), and assuming that $\mathsf{A}{\leftrightarrow}\mathsf{M}_i$ PT are the only dissipative processes under isothermal conditions, we obtain

$$D = \sum_{i=1}^{m}\left(\boldsymbol{P}^T\!:\!\frac{\partial \boldsymbol{F}}{\partial c_i} - \frac{\partial \psi}{\partial c_i}\right)\dot{c}_i = \sum_{i=1}^{m} \tilde{X}_{i0}\dot{c}_i \tag{33}$$

with

$$\tilde{X}_{i0} = \boldsymbol{P}^T{\cdot}\boldsymbol{F}_e\!:\!\boldsymbol{\varepsilon}_{ti} - \frac{J_t}{2}\boldsymbol{E}_e\!:\!(\boldsymbol{C}_i - \boldsymbol{C}_0)\!:\!\boldsymbol{E}_e - \frac{J_t}{2}(\boldsymbol{E}_e\!:\!\boldsymbol{C}(c)\!:\!\boldsymbol{E}_e)\boldsymbol{F}_t^{-1}\!:\!\boldsymbol{\varepsilon}_{ti} - \Delta\psi^\theta. \tag{34}$$

Expressions for $\tilde{X}_{i0}$ are equal to X_{i0} from Eq. $(17)_1$ without terms related to the interaction energy ψ^{in}. This is natural because the mixture rule $(32)_2$ neglects interactions. Since $\psi^{in} = 0$ in complete A and M, it should not participate in X_Σ. Next, we equal the dissipation rates

$$D = \sum_{i=1}^{m} \tilde{X}_{i0}\dot{c}_i = X_\Sigma \dot{c}. \tag{35}$$

To reduce m degrees of freedom c_i to the single one c, one has to assume a noncontradictory path in c_i space that excludes variant-variant transformations. We transform

$$D = \sum_{i=1}^{m} \tilde{X}_{i0}\dot{c}_i = \sum_{i=1}^{m} c_i\tilde{X}_{i0}\frac{\dot{c}_i}{c_i} \tag{36}$$

and assume that $\dot{c}_i = \nu c_i$, where ν is a parameter independent of i, which is determined from

$$\dot{c} = \sum_{i=1}^{m}\dot{c}_i = \nu\sum_{i=1}^{m} c_i = \nu c \quad \rightarrow \quad \nu = \frac{\dot{c}}{c}. \tag{37}$$

Substituting Eq. (37) in Eqs. (35) and (36), we obtain

$$X_\Sigma = \sum_{i=1}^{m}\frac{c_i}{c}\tilde{X}_{i0} = \sum_{i=1}^{m}\tilde{c}_i\tilde{X}_{i0} = \boldsymbol{P}^T{\cdot}\boldsymbol{F}_e\!:\!\boldsymbol{\varepsilon}_{tM} - \frac{J_t}{2}\boldsymbol{E}_e\!:\!(\boldsymbol{C}_M - \boldsymbol{C}_0)\!:\!\boldsymbol{E}_e - \frac{J_t}{2}(\boldsymbol{E}_e\!:\!\boldsymbol{C}(c)\!:\!\boldsymbol{E}_e)\boldsymbol{F}_t^{-1}\!:\!\boldsymbol{\varepsilon}_{tM} - \Delta\psi^\theta;$$
$$\boldsymbol{\varepsilon}_{tM} = \sum_{i=1}^{m}\tilde{c}_i\varepsilon_{ti}; \qquad \boldsymbol{C}_M = \sum_{i=1}^{m}\tilde{c}_i\boldsymbol{C}_i, \tag{38}$$

where $\tilde{c}_i = c_i/c$ is the volume fraction of M_i within martensitic mixture, $\sum_{i=1}^{m}\frac{c_i}{c} = 1$. Then the phase equilibrium Eq. (29) is

$$X_\Sigma = \sum_{i=1}^{m}\tilde{c}_i\tilde{X}_{i0} = \boldsymbol{P}^T{\cdot}\boldsymbol{F}_e\!:\!\boldsymbol{\varepsilon}_{tM} - \frac{J_t}{2}\boldsymbol{E}_e\!:\!(\boldsymbol{C}_M - \boldsymbol{C}_0)\!:\!\boldsymbol{E}_e - \frac{J_t}{2}(\boldsymbol{E}_e\!:\!\boldsymbol{C}(c)\!:\!\boldsymbol{E}_e)\boldsymbol{F}_t^{-1}\!:\!\boldsymbol{\varepsilon}_{tM} - \Delta\psi^\theta = \sum_{i=1}^{m}\tilde{c}_i k_{0-i}. \tag{39}$$

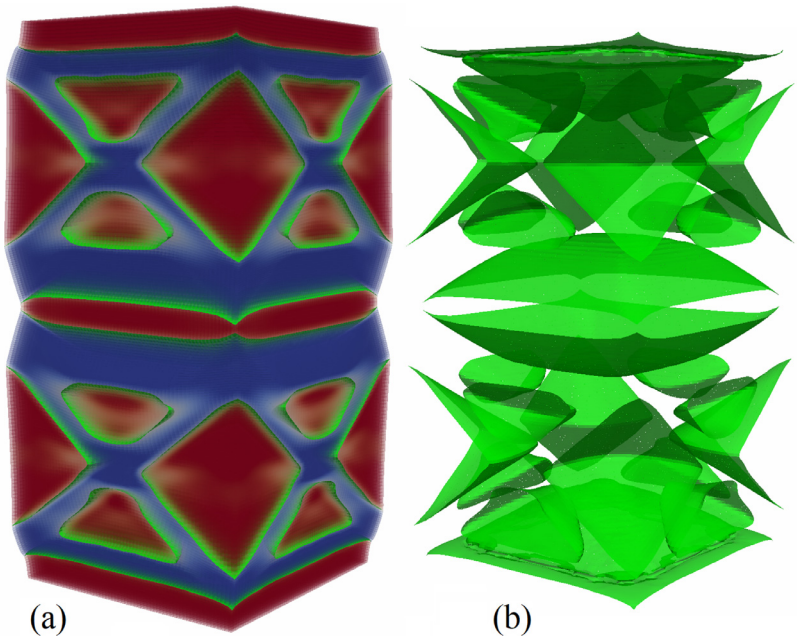

Fig. 13. Distribution of volume fraction of austenite (red) and martensite (blue) with traces of isosurfaces on which the phase equilibrium condition (39) is satisfied (a) and the isosurfaces on which the phase equilibrium condition (39) is met (b). (For interpretation of the references to color in this figure legend, the reader is referred to the web version of this article.)

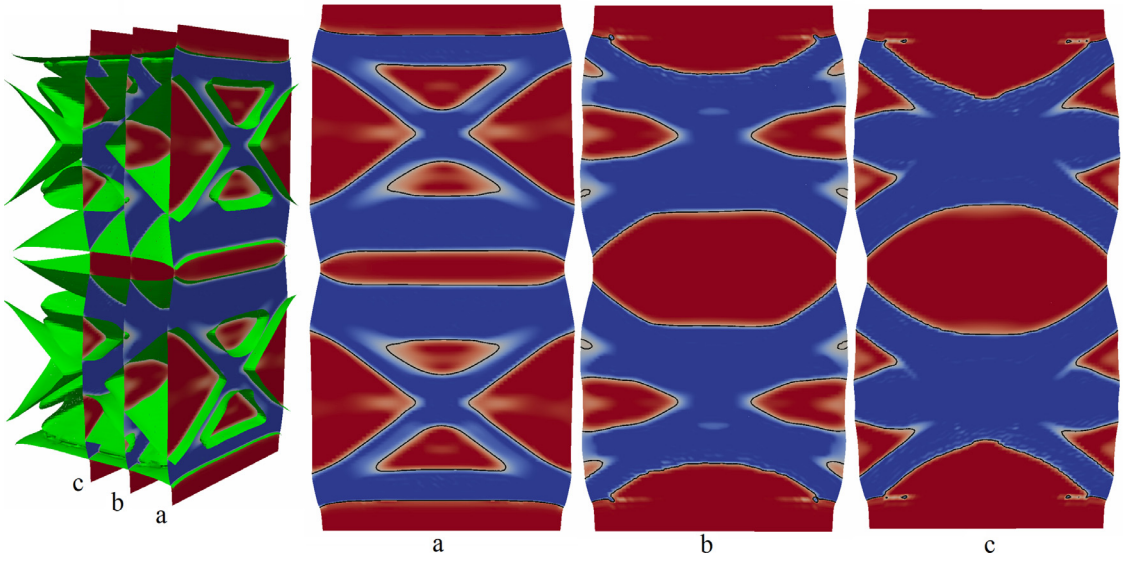

Fig. 14. Three 2D slices of the solution for fields of the volume fraction of austenite (red) and martensite (blue). Black lines correspond to the phase equilibrium condition (39) and coincide with the stationary interfaces. (For interpretation of the references to color in this figure legend, the reader is referred to the web version of this article.)

After a stationary solution is reached, all fields in Eq. (39) are known, and the isosurfaces, on which condition (39) is locally satisfied, are shown in Fig. 13. To obtain a closer observation inside the sample, we consider three slices of the solution with the overlaid isosurfaces (39). The overlap of the isosurfaces with the slices of the solution are shown with black isolines in Fig. 14. It can be clearly seen that the phase equilibrium condition (39) is met at the stationary interfaces. Previously, a similar result was obtained for 2D small-strain problems without athermal thresholds and single variant within nanoscale PFA(Javanbakht and Levitas, 2015; Javanbakht and Levitas, 2016; Javanbakht and Levitas, 2018; Levitas and Javanbakht, 2014) and two variants within microscale PFA (Esfahani et al., 2020; Levitas et al., 2018) with a simplified expression for X_Σ. Here, we derived and applied a general expression (39) for the phase equilibrium condition with different and variable athermal thresholds for m variants, for large strain, and 3D problem. Note that Eq. (39), in particular, means that neglecting gradient

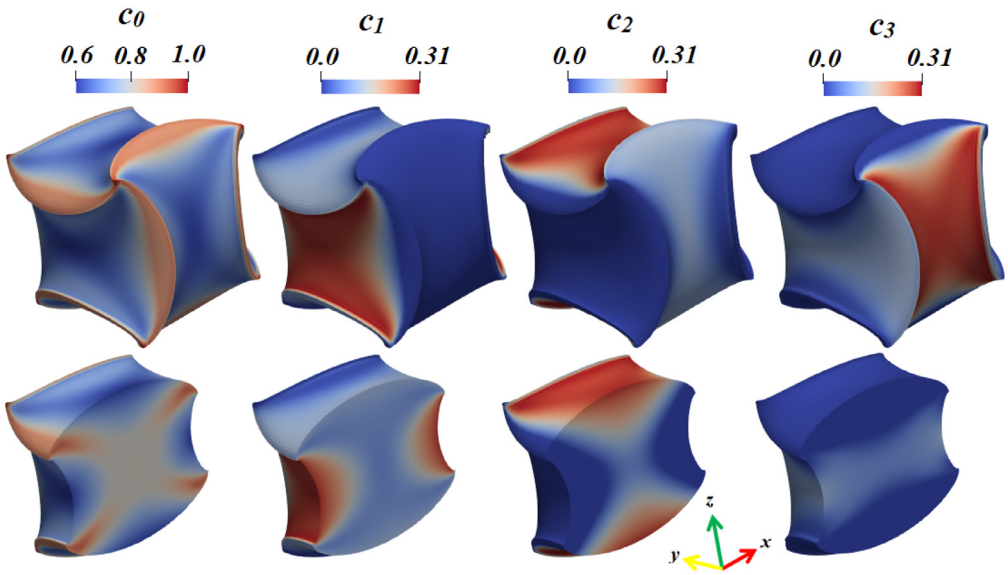

Fig. 15. Solutions for the volume fraction of Si II variants and Si I obtained under hydrostatic loading slightly exceeding 12 GPa. Upper row shows the entire sample and the lower row shows the sample cut in half for visualization of the interior.

energy does not introduce an additional athermal threshold to the interface propagation, similar to the traditional nanoscale model with gradient energy. The reason is that in a computational, completely formed interface, which is usually one finite element thick, large gradients of volume fraction of martensitic variants and transformation strain leads to a high elastic and interaction energy, which plays a role of an effective gradient and interface energy. That is why the stationary microstructurs for nanoscale and scale-free models are similar. This was directly shown for small strains with neglected athermal threshold and 2D formulation in Esfahani et al. (2020)

6.6. Hydrostatic loading

The PT pressure for Si I → Si II under the hydrostatic loading was calibrated to 12 GPa. To examine the PT process under hydrostatic loading, we consider a cubic sample whose three external cubic faces have zero out of plane displacements and zero shear stresses, acting as the symmetry planes. After we apply compressive stress slightly exceeding 12 GPa on the other three faces, realizing a hydrostatic loading condition, PT starts and continues up to the state with the volume fraction of each variant not exceeding 0.31 and the volume fraction of mixture of martensitic variants not exceeding 0.4. Then solution diverges due to large geometric changes near edges, where PT does not occur. The large distortions along the edges of the sample are caused by the large compressive transformation strains (-0.447) for three martensitic variants in corresponding spatial directions, while regions near edges do not transform. The final solution fields for the entire sample after mirroring with respect to the symmetry planes of the simulation fields are shown in Fig. 15. It can be seen that each of the three martensitic variants equally occupies some regions of the sample close to the external faces in their corresponding spatial directions.

7. Concluding remarks

The scale-free PFA developed in Levitas et al. (2004) and Idesman et al. (2005) for small strains was essentially generalized to a fully geometrically nonlinear formulation with finite elastic and transformation strains and lattice rotation, as well as anisotropic and different elastic properties of phases. Introducing the interface energy in an average sense instead of the traditional gradient energy in the Helmholtz free energy makes the model local and scale-independent. The strain-softening and corresponding transformation strain localization is achieved using an interaction-free energy term, which leads to a discrete martensitic microstructure. The model tracks only finite-width interfaces between austenite and the mixture of martensitic variants and does not consider the interfaces between martensitic variants.

Recent atomistic simulations (Levitas et al., 2017b; Zarkevich et al., 2018) show that the PT conditions for Si I↔Si II PTs are linear functions of stresses normal to the cubic faces of Si I, and represent planes in 3D normal stress space, which are not parallel and intersect along some line. The presence of dislocations changes the numerical value of transformation stresses but does not change these properties; see Babaei and Levitas (2019). Previous microscale and scale-free theories could not describe these results. We included these results by assuming that the effective threshold for PTs k_{i-0} is dependent on normal to cubic faces stresses and volume fraction of martensitic variant, and thus is different for direct and reverse PTs. These dependencies are calibrated based on the PT conditions for Si I↔Si II PTs.

Due to large transformation strains and the Si I↔Si II PT conditions obtained by experiments, it appears that fitting to experiment is possible when the athermal threshold for PTs k_{i-0} is not only positive but might be negative for large compressive stresses $0.5(\sigma_1+\sigma_2)$. That means that $\mathsf{A} \rightarrow \mathsf{M}_i$ PT starts in the region of stability of A and dissipation rate is negative, i.e., there is a formal violation of the second law of thermodynamics. This issue is discussed in detail. First, many experimental results demonstrate that under plastic straining, the PT may occur at a pressure well below than the phase equilibrium pressure (Blank and Estrin, 2013; Gao et al., 2019; Pandey and Levitas, 2020). Such a counterintuitive behavior was explained in Levitas (2004), Javanbakht and Levitas (2015, 2018), Levitas et al. (2018) and Esfahani et al. (2020) by strong stress tensor concentration produced by defects induced by plastic deformation, e.g., dislocation pileups. This means that our formal contradiction with thermodynamics would disappear if we would introduce defects explicitly rather than incorporated in the threshold k_{i-0}. That is why we accept that within our simplified theory k_{i-0} may be negative for some combination of stresses, but the net thermodynamic driving force $X_{net} = X_{i0} - k_{i-0} > 0$. To include this possibility, we introduced the concept of the effective threshold that include promoting effect of the defects instead of the positive athermal threshold.

In the previous modeling of PTs in Si I, Si II was considered as a single variant. However, twinned (i.e., multivariant) Si II was recently observed in Popov et al. (2015) during Si I → Si II PT under hydrostatic loading. Here we presented the first modeling and simulations results for Si I → multivariant Si II PT.

Computational procedures and numerical algorithms are implemented using the deal.II FEM program library. The main challenges are related to large transformation strains, which vary from zero to its maximum magnitude within numerous phase interfaces with a width of a single finite element. Multiple 3D problems are solved to study the effects of mesh size, holding time during quasi-static loading, and strain rate on the microstructure evolution during Si I↔Si II PTs. Previously, 2D problems were solved within a scale-free model for small strains in Levitas et al. (2004), Idesman et al. (2005) and Esfahani et al. (2020, 2018). While uniaxial compressive loading promotes the appearance of the variant M_1 and suppresses two other variants, internal stresses caused by M_1 leads to the appearance of M_2 and M_3 with $c_i < 0.3$. In most cases, M_2 and M_3 disappear from the final fully transformed Si II regions. Thus, they play the role of intermediate phases, which appear to relax energy at the intermediate stages but disappear at the end.

Finite strain formulation allowed us to reproduce large and heterogeneous crystal lattice rotation, leading to differently oriented grains divided by diffuse grain boundaries. This results in the transformation of a single crystal Si I into polycrystal, as observed in experiments in Popov et al. (2015), and the cubic lattice is not aligned with the uniaxial compression everywhere and requires larger compressive stresses for transformation. However, in the regions where both cubic and tetragonal lattices are aligned along the coherent interfaces, the lattice of Si I is elastically extended along the interface, which promotes PT. This extension reduces while moving from interfaces into the bulk Si I. Due to different surroundings, different Si II regions have different orientations as well. This explains "polycrystalline nature" of the Si II obtained from the single-crystal Si I experimentally in Popov et al. (2015). However, the final Si II is a homogeneous single crystal without lattice rotations. Thus, lattice rotations in Si I and Si II represent an additional mechanism of stress relaxation at intermediate transformations stages, which disappear in the final product, similar to variants M_2 and M_3.

Although finer mesh produces a more detailed microstructure, the solution becomes practically mesh-independent after a mesh size is 80 times smaller than the sample size. For solutions close to the stationary ones, small Si II regions coalesce, microstructure loses its symmetry with respect to the vertical plane and tends to broad bands. For rough mesh, such a solution appears at very early stages of straining. That is why rough mesh allows one to reproduce microstructures close to the stationary ones much more effectively because it does not reproduce fine details from the beginning.

For quasi-static loading, increasing holding time between strain increments leads to a more completed PT and microstructure with fewer bands and interfaces, i.e., coalescence and change in morphology and orientation occur driven by minimization of the internal elastic-stress energy and interfacial energy. The microstructure changes from separated partially transformed martensitic regions to larger almost or fully transformed martensitic bands. Change in morphology means that in some regions reverse PT occurs at continuous compression, despite large transformation hysteresis. The stress-strain curve for the longer holding time is below the curves for the shorter holding time.

When microstructure from the upper and lower parts of a sample coalesce, large increment in the amount of Si II and in corresponding transformation strain leads to a large drop of the Cauchy stress. With an increase of the holding time, the prescribed strain at which the coalescence and drop starts, reduces. This is related mostly to a larger amount of residual Si II near the top and bottom surfaces of the sample. After further loading of Si II, the nonlinear curve for the longest holding time is caused by further PT progress and variant-variant transformation under growing stresses.

A similar sequence of the stress-strain curves is observed with a reduction of the strain rate (which gives more time for PT progress) for the beginning of the PT. With further straining, stress-strain curves exhibit the Maxwell stress plateau lifted up by the effective threshold, with practically the same stress for all strain rates. Thus, for all considered strain rates, the growth rate of Si II is sufficient to support PT at stress close to that for the quasi-equilibrium loading. Coalescence of the microstructure near the horizontal symmetry plane leads to stress drops similar to quasi-static loading, but it is smaller for high strain rate due to smaller increments in the amount of Si II. For the intermediate strain rate, stress drop starts approximately at the same strain as for two other strain rate, but it is spread over the larger strain interval due to different topology of the microstructure near the symmetry plane.

Expressions for the driving force for an interface propagation and conditions for the interface equilibrium were derived and applied for the large strain, 3D formulation, and for different variable athermal thresholds for m variants. It is shown

that for the majority of the stationary interfaces, local thermodynamic equilibrium conditions (thermodynamic driving force for the interface motion equal to the effective threshold) is satisfied. For a scale-free model, such result was obtained previously for 2D small-strain problems without athermal thresholds and single variant within nanoscale PFA (Javanbakht and Levitas, 2015; Javanbakht and Levitas, 2016; Javanbakht and Levitas, 2018; Levitas and Javanbakht, 2014) and two variants within microscale PFA (Esfahani et al., 2020; Levitas et al., 2018) with a simplified expression for X_Σ. This result is nontrivial and shows that despite the dropping gradient energy, the current model exhibits equilibrium properties of interfaces similar to traditional nanoscale models (Javanbakht and Levitas, 2015; 2016; 2018; Levitas and Javanbakht, 2014), i.e., it does not produce an additional athermal threshold. The reason is that in computations, a completely formed interface, which is usually one finite element thick, large gradients of volume fraction of martensite and transformation strain lead to significant interaction and elastic energies, reproducing an effective gradient and interface energy.

Under hydrostatic loading, all three martensitic variants appear in equal portions in different, symmetry-related places of a sample. PT continues up to the state with the volume fraction of each variant not exceeding 0.31 and the volume fraction of mixture of martensitic variants not exceeding 0.4. Then solution diverges due to large geometric changes near nontransforming edges. We will try to overcome divergence by promoting nucleation in the middle part of the sample due to introduced defects, which may reduce or postpone large geometric changes near edges and divergence of a solution.

A similar approach can be applied to other PTs accompanied by large transformation strain (e.g., graphite to diamond and graphite-like (hexagonal or rhombohedral) boron nitride to diamond-like (wurtzitic or cubic) superhard boron nitride). As the next step, the PT should be combined with the discrete localized plastic flow (e.g., shear bands and dislocation pileups) (Esfahani et al., 2020; 2018; Levitas et al., 2018) in order to study plastic strain-induced PTs. Besides, this approach can be generalized for multiphase materials, which is especially important for Si, which has more than a dozen phases.

Declaration of Competing Interest

The authors declare that they have no known competing financial interests or personal relationships that could have appeared to influence the work reported in this paper.

CRediT authorship contribution statement

Hamed Babaei: Methodology, Software, Formal analysis, Writing - original draft, Visualization. **Valery I. Levitas:** Conceptualization, Methodology, Formal analysis, Resources, Writing - review & editing, Supervision, Project administration, Funding acquisition.

Acknowledgements

The support of NSF (CMMI-1943710 and MMN-1904830), ONR (N00014-16-1-2079), ARO (GS100000183W911NF-17-1-0225), and Iowa State University (Vance Coffman Faculty Chair Professorship) is gratefully acknowledged. The simulations were performed at Extreme Science and Engineering Discovery Environment (XSEDE), allocation TG-MSS170015.

Supplementary material

Supplementary material associated with this article can be found, in the online version, at doi:10.1016/j.jmps.2020.104114.

References

Arghavani, J., Auricchio, F., Naghdabadi, R., Reali, A., Sohrabpour, S., 2010. A 3-d phenomenological constitutive model for shape memory alloys under multiaxial loadings. Int. J. Plast. 26 (7), 976–991.
Artemev, A., Jin, Y., Khachaturyan, A., 2001. Three-dimensional phase field model of proper martensitic transformation. Acta Mater. 49 (7), 1165–1177.
Artemev, A., Wang, Y., Khachaturyan, A., 2000. Three-dimensional phase field model and simulation of martensitic transformation in multilayer systems under applied stresses. Acta Mater. 48 (10), 2503–2518.
Babaei, H., Levitas, V.I., 2018. Phase-field approach for stress-and temperature-induced phase transformations that satisfies lattice instability conditions. Part II. Simulations of phase transformations Si I↔Si II. Int. J. Plast. 107, 223–245.
Babaei, H., Levitas, V.I., 2019. Effect of 60° dislocation on transformation stresses, nucleation, and growth for phase transformations between silicon I and silicon II under triaxial loading: phase-field study. Acta Mater. 177, 178–186.
Bangerth, W., Hartmann, R., Kanschat, G., 2007. Deal. Ila general-purpose object-oriented finite element library. ACM Transactions on Mathematical Software (TOMS) 33 (4), 24–es.
Basak, A., Levitas, V.I., 2017. Interfacial stresses within boundary between martensitic variants: analytical and numerical finite strain solutions for three phase field models. Acta Mater. 139, 174–187.
Basak, A., Levitas, V.I., 2018. Nanoscale multiphase phase field approach for stress-and temperature-induced martensitic phase transformations with interfacial stresses at finite strains. J. Mech. Phys. Solids 113, 162–196.
Beissel, S., Belytschko, T., 1996. On patterns of deformation in phase transformations and lüders bands. Int. J. Solids Struct. 33 (12), 1689–1707.
Blank, V.D., Estrin, E.I., 2013. Phase Transitions in Solids Under High Pressure. Crc Press.
Budnitzki, M., Kuna, M., 2016. Stress induced phase transitions in silicon. J. Mech. Phys. Solids 95, 64–91.
Buryachenko, V., 2007. Micromechanics of Heterogeneous Materials. Springer Science & Business Media.
Chen, H., Zarkevich, N.A., Levitas, V.I., Johson, D.D., Zhang, X., 2020. Fifth-degree elastic potential for predictive stress-strain relations and elastic instabilities under large strain and complex loading in Si. NPJ Computational Materials 6, 115.
Chen, L.Q., Shen, J., 1998. Applications of semi-implicit fourier-spectral method to phase field equations. Comput. Phys. Commun. 108 (2–3), 147–158.
Clayton, J.D., Knap, J., 2011. A phase field model of deformation twinning: nonlinear theory and numerical simulations. Physica D 240 (9–10), 841–858.

Domnich, V., Ge, D., Gogotsi, Y., 2004. Indentation-induced phase transformations in semiconductors. High Press. Surf Sci. Eng.; Section 5.1 381–442.
Esfahani, S.E., Ghamarian, I., Levitas, V.I., 2020. Strain-induced multivariant martensitic transformations: a scale-independent simulation of interaction between localized shear bands and microstructure. Acta Mater. 196, 430–433.
Esfahani, S.E., Ghamarian, I., Levitas, V.I., Collins, P.C., 2018. Microscale phase field modeling of the martensitic transformation during cyclic loading of NiTi single crystal. Int. J. Solids Struct. 146, 80–96.
Gao, Y., Ma, Y., An, Q., Levitas, V., Zhang, Y., Feng, B., Chaudhuri, J., Goddard III, W.A., 2019. Shear driven formation of nano-diamonds at sub-gigapascals and 300 k. Carbon 146, 364–368.
Ghosh, G., Olson, G.B., 1994a. Kinetics of fcc bcc heterogeneous martensitic nucleationI. The critical driving force for athermal nucleation. Acta Metall. Mater. 42 (10), 3361–3370.
Ghosh, G., Olson, G.B., 1994b. Kinetics of FCC BCC heterogeneous martensitic nucleation II. Thermal activation. Acta Metall. Mater. 42 (10), 3371–3379.
Grinfeld, M., 1991. Thermodynamic Methods in the Theory of Heterogeneus Systems. Longman Scientific and Technical.
Grujicic, M., Olson, G., Owen, W., 1985. Mobility of martensitic interfaces. Metall. Trans. A 16 (10), 1713–1722.
Gupta, M.C., Ruoff, A.L., 1980. Static compression of silicon in the [100] and in the [111] directions. J. Appl. Phys. 51 (2), 1072–1075.
Hu, J.Z., Merkle, L.D., Menoni, C.S., Spain, I.L., 1986. Crystal data for high-pressure phases of silicon. Phys. Rev. B 34 (7), 4679.
Idesman, A., Levitas, V., Preston, D., Cho, J.-Y., 2005. Finite element simulations of martensitic phase transitions and microstructures based on a strain softening model. J. Mech. Phys. Solids 53 (3), 495–523.
Idesman, A.V., Cho, J.-Y., Levitas, V.I., 2008. Finite element modeling of dynamics of martensitic phase transitions. Appl. Phys. Lett. 93 (4), 043102.
Javanbakht, M., Levitas, V.I., 2015. Interaction between phase transformations and dislocations at the nanoscale. Part 2: Phase field simulation examples. J. Mech. Phys. Solids 82, 164–185.
Javanbakht, M., Levitas, V.I., 2016. Phase field simulations of plastic strain-induced phase transformations under high pressure and large shear. Phys. Rev. B 94 (21), 214104.
Javanbakht, M., Levitas, V.I., 2018. Nanoscale mechanisms for high-pressure mechanochemistry: a phase field study. J. Mater. Sci. 53 (19), 13343–13363.
Jiang, D., Kyriakides, S., Landis, C.M., 2017. Propagation of phase transformation fronts in pseudoelastic NiTi tubes under uniaxial tension. Extreme Mech. Lett. 15, 113–121.
Jiang, D., Kyriakides, S., Landis, C.M., Kazinakis, K., 2017. Modeling of propagation of phase transformation fronts in NiTi under uniaxial tension. Eur. J. Mech.-A/Solids 64, 131–142.
Kim, S.G., Kim, D.I., Kim, W.T., Park, Y.B., 2006. Computer simulations of two-dimensional and three-dimensional ideal grain growth. Phys. Rev. E 74 (6), 061605.
Lagoudas, D., Hartl, D., Chemisky, Y., Machado, L., Popov, P., 2012. Constitutive model for the numerical analysis of phase transformation in polycrystalline shape memory alloys. Int. J. Plast. 32, 155–183.
Lekhnitskii, S.G., 1963. Theory of Elasticity of an Anisotropic Elastic Body. Holden-Day.
Levitas, V.I., 1994. Thermomechanical description of pseudoelasticity: the threshold-type dissipative force with discrete memory. Mech. Res. Commun. 21 (3), 273–280.
Levitas, V.I., 1995. The postulate of realizability: Formulation and applications to the post-bifurcation behaviour and phase transitions in elastoplastic materials-Part 1. Int. J. Eng. Sci. 33 (7), 947–971.
Levitas, V.I., 1995. The postulate of realizability: formulation and applications to the post-bifurcation behaviour and phase transitions in elastoplastic materials-Part 2. Int. J. Eng. Sci. 33 (7), 921–945.
Levitas, V.I., 1996. Some relations for finite inelastic deformation of microheterogeneous materials with moving discontinuity surfaces. In: IUTAM Symposium on Micromechanics of Plasticity and Damage of Multiphase Materials. Springer, pp. 313–320.
Levitas, V.I., 2004. High-pressure mechanochemistry: conceptual multiscale theory and interpretation of experiments. Phys. Rev. B 70 (18), 184118.
Levitas, V.I., 2018. Phase field approach for stress-and temperature-induced phase transformations that satisfies lattice instability conditions. Part I. General theory. Int. J. Plast. 106, 164–185.
Levitas, V.I., Chen, H., Xiong, L., 2017. Lattice instability during phase transformations under multiaxial stress: modified transformation work criterion. Phys. Rev. B 96 (5), 054118.
Levitas, V.I., Chen, H., Xiong, L., 2017. Triaxial-stress-induced homogeneous hysteresis-free first-order phase transformations with stable intermediate phases. Phys. Rev. Lett. 118 (2), 025701.
Levitas, V.I., Esfahani, S.E., Ghamarian, I., 2018. Scale-free modeling of coupled evolution of discrete dislocation bands and multivariant martensitic microstructure. Phys. Rev. Lett. 121 (20), 205701.
Levitas, V.I., Idesman, A.V., Preston, D.L., 2004. Microscale simulation of martensitic microstructure evolution. Phys. Rev. Lett. 93 (10), 105701.
Levitas, V.I., Javanbakht, M., 2014. Phase transformations in nanograin materials under high pressure and plastic shear: nanoscale mechanisms. Nanoscale 6 (1), 162–166.
Levitas, V.I., Levin, V.A., Zingerman, K.M., Freiman, E.I., 2009. Displacive phase transitions at large strains: phase-field theory and simulations. Phys. Rev. Lett. 103 (2), 025702.
Levitas, V.I., Preston, D.L., 2002. Three-dimensional landau theory for multivariant stress-induced martensitic phase transformations. I. Austenite martensite. Phys. Rev. B 66 (13), 134206.
Levitas, V.I., Preston, D.L., 2002. Three-dimensional landau theory for multivariant stress-induced martensitic phase transformations. II. Multivariant phase transformations and stress space analysis. Phys. Rev. B 66 (13), 134207.
Levitas, V.I., Roy, A.M., 2016. Multiphase phase field theory for temperature-induced phase transformations: formulation and application to interfacial phases. Acta Mater 105, 244–257.
Levitas, V.I., Roy, A.M., Preston, D.L., 2013. Multiple twinning and variant-variant transformations in martensite: phase-field approach. Phys. Rev. B 88 (5), 054113.
Mandel, J., 1966. Contribution théorique à létude de lécrouissage et des lois de lécoulement plastique. In: Applied Mechanics. Springer, pp. 502–509.
Pandey, K., Levitas, V.I., 2020. In situ quantitative study of plastic strain-induced phase transformations under high pressure: Example for ultra-pure Zr. Acta Mater. 196, 338–346.
Panico, M., Brinson, L.C., 2007. A three-dimensional phenomenological model for martensite reorientation in shape memory alloys. J. Mech. Phys. Solids 55 (11), 2491–2511.
Popov, D., Park, C., Kenney-Benson, C., Shen, G., 2015. High pressure laue diffraction and its application to study microstructural changes during the $\alpha\beta$ phase transition in si. Rev. Sci. Instrum. 86 (7), 072204.
Schall, J.D., Gao, G., Harrison, J.A., 2008. Elastic constants of silicon materials calculated as a function of temperature using a parametrization of the second-generation reactive empirical bond-order potential. Phys. Rev. B 77 (11), 115209.
Schneider, D., Tschukin, O., Choudhury, A., Selzer, M., Böhlke, T., Nestler, B., 2015. Phase-field elasticity model based on mechanical jump conditions. Comput. Mech. 55 (5), 887–901.
Shaw, J.A., 2000. Simulations of localized thermo-mechanical behavior in a NiTi shape memory alloy. Int. J. Plast. 16 (5), 541–562.
Steinbach, I., 2009. Phase-field models in materials science. Modell. Simul. Mater. Sci. Eng. 17 (7), 073001.
Steinbach, I., Apel, M., 2006. Multi phase field model for solid state transformation with elastic strain. Physica D 217 (2), 153–160.
Steinbach, I., Pezzolla, F., Nestler, B., Seeßelberg, M., Prieler, R., Schmitz, G.J., Rezende, J.L., 1996. A phase field concept for multiphase systems. Physica D 94 (3), 135–147.
Tóth, G.I., Pusztai, T., Gránásy, L., 2015. Consistent multiphase-field theory for interface driven multidomain dynamics. Phys. Rev. B 92 (18), 184105.

Tuma, K., Stupkiewicz, S., 2016. Phase-field study of size-dependent morphology of austenite–twinned martensite interface in cualni. Int. J. Solids Struct. 97, 89–100.
Tuma, K., Stupkiewicz, S., Petryk, H., 2016. Size effects in martensitic microstructures: finite-strain phase field model versus sharp-interface approach. J. Mech. Phys. Solids 95, 284–307.
Voronin, G., Pantea, C., Zerda, T., Wang, L., Zhao, Y., 2003. In situ x-ray diffraction study of silicon at pressures up to 15.5 GPa and temperatures up to 1073 k. Phys. Rev. B 68 (2), 020102.
Wang, Y., Khachaturyan, A., 1997. Three-dimensional field model and computer modeling of martensitic transformations. Acta Mater. 45 (2), 759–773.
Zaki, W., Moumni, Z., 2007. A three-dimensional model of the thermomechanical behavior of shape memory alloys. J. Mech. Phys. Solids 55 (11), 2455–2490.
Zarkevich, N.A., Chen, H., Levitas, V.I., Johnson, D.D., 2018. Lattice instability during solid-solid structural transformations under a general applied stress tensor: example of si idelSsi II with metallization. Phys. Rev. Lett. 121 (16), 165701.
Zeng, Z., Zeng, Q., Ge, M., Chen, B., Lou, H., Chen, X., Yan, J., Yang, W., Mao, H.-k., Yang, D., et al., 2020. Origin of plasticity in nanostructured silicon. Phys. Rev. Lett. 124 (18), 185701.
Zhu, J., Gao, Y., Wang, D., Zhang, T.-Y., Wang, Y., 2017. Taming martensitic transformation via concentration modulation at nanoscale. Acta Mater. 130, 196–207.
Ziegler, H., 1977. An Introduction to Thermomechanics. North-Holland, Amsterdam.